

A comparative study of split advection algorithms on Moment-of-Fluid (MOF) method for incompressible flow

Zhouteng Ye^a

^a Ocean College, Zhejiang University, Zhoushan 316021, Zhejiang, People's Republic of China

Abstract

The moment-of-fluid method (MOF) is known as an extension of the volume-of-fluid method with piecewise linear interface construction (VOF-PLIC). In this study, several directional splitting advection algorithms are extended from the VOF-PLIC method to the MOF method. Those methods, along with some existing directional splitting algorithms, are presented in detail, especially on the geometrical and non-geometrical nature of the advection algorithm. Besides, we also proposed a simple and efficient analytic form to calculate the volume and centroid of the intersection polyhedron in 3D. Several numerical tests, including both 2D and 3D tests, are carried out to investigate mass conservation and geometrical error. Numerical results suggest that the mixed EI and LE scheme (EILE2D) [1] has the best overall performance in 2D and Weymouth and Yue's scheme (WY) has the best overall performance in 3D.

Keywords: Moment-of-Fluid method, Advection algorithms, Interface tracking, Volume tracking

1. Introduction

The volume of fluid method (VOF) has become one of the most popular techniques in tracking the interface between different materials. In the past 45 years, a variety of VOF methods has been developed [2, 3, 4, 5, 5, 6] Among those VOF methods, the volume-of-fluid method with piece-wise line interface construction (VOF-PLIC) is one of the most widely used in tracking the interface within the Eulerian framework. Dyadechko and Shashkov [7] developed Moment-of-Fluid method (MOF) as an extension of VOF-PLIC method. With the centroid of the fluid as an additional constraint, the MOF method resolves the interface with a smaller minimum scale than the VOF-PLIC algorithm and has been extended from Cartesian grid to multiple frameworks such as adaptive mesh refinement(AMR)[8, 9, 10], arbitrary Lagrangian-Eulerian (ALE) [11, 12].

The MOF method contains two parts: (1) reconstruction algorithm and, (2) advection algorithm. The reconstruction algorithm in MOF method is to use the known reference centroid and volume fraction to find the optimized linear cut-off in a cell. Unlike VOF-PLIC method, the MOF reconstruction does not need the information from the neighbouring grids, which provides a better resolution when there is insufficient from the neighbouring grid. Since the Dyadechko and Shashkov [7] proposed the first MOF reconstruction algorithm, several improvements has been

Email address: yzt9zju@gmail.com (Zhouteng Ye)

done [8, 9, 13, 14, 15]. In 2D Cartesian grid, the analytic solution to the reconstruction is proposed by Lemoine et al. [14]. Unfortunately, the 2D analytic solution cannot be extended to 3D. In 3D, Milcent and Lemoine [15] proposed an analytic form of the gradient when calculating the normal vector in MOF reconstruction. Unlike the full analytic solution in 2D, the 3D algorithm estimates the normal vector with iteration algorithm. Note that in this study, the reconstruction algorithm in this study follows the algorithm of Lemoine et al. [14] (in 2D) and the algorithm of Milcent and Lemoine [15] (in 3D).

Extended from VOF advection [16], the MOF advection can also be implemented either with operator split [9, 17, 18] or unsplit algorithm [19, 11, 12], with an additional advection step of the centroid. Dyadechko and Shashkov [7] show that the material centroid in the incompressible flow move similarly to Lagrangian particles and makes it a perfect choice for interface reconstruction input. Unsplit methods have the advantage of only requiring one advection and reconstruction step per time step, the advection step is often algorithmically complex Scardovelli and Zaleski [20]. Split methods takes the advantage of the simple geometry of the Cartesian grid, making the flux calculation simple and efficient. Some simple and efficient formulation for the polyhedron intersection on Cartesian has been proposed Scardovelli and Zaleski [21], Milcent and Lemoine [15].

There are some known issues on split advection algorithms, especially on the mass conservation [16]. For a divergence-free flow field, the discretized velocity field at intermediate time step as not necessarily divergence-free. The divergence correction term [22] helps to improve the local and global mass conservation. The divergence correction term is expressed either in geometrical for non-geometrical approach. Aulisa et al. [1] show the geometrical properties of the flux-correction term for Eulerian Implicit (EI) and Lagrangian Explicit (LE) schemes and suggest using a hybrid EI and LE scheme helps improve the accuracy and mass conservation. The geometrical approach can be naturally extended to split MOF advection, as the centroid can be determined directly from the corresponding geometrical expression Jemison et al. [9]. The hybrid EI and LE scheme in 2D (EILE2D) [1] is both geometrical preserving and area preserving, and has been extended to MOF method [23, 18]. The extension of EILE2D to 3D is not direct, Aulisa et al. [24] composites the 3D velocity field into 3 2D velocity fields. however, this decomposition strategy may cause stability issue in practical simulation. Besides, the hybrid EI and LE scheme in 3D has not been extended to MOF advection. Other approaches deals with the divergence-correction term with an algebraic correction. Weymouth and Yue [25] enforced the divergence-correction term with either 0 or 1, depending on the initial value of the volume fraction. This approach is ultimately mass conservation, however, not geometrical preserving. This approach has been extended to MOF advection, with the centroids advection in a way that used in EI schemes [23, 18]. Another non-geometrical correction introduces an Eulerian Algebraic (EA) step between the EI and LE scheme (Namely EIEALE scheme) [26]. Again, the intermediate Eulerian Algebraic does not guarantee geometrical preserving and has not yet been extended to MOF advection.

In this comparative study, we investigates the accuracy and mass conservation properties of different split MOF advection methods. Besides the existing EI, LE, EILE2D [1, 9] and WY schemes [25, 23, 18], we also extend the EILE3D (Eulerian Implicit Lagrangian Explicit in 3D) [24], , EILE3DS (EILE3D simplified) [24], EIEALE (EI-EA-

LE) scheme [26] to from VOF-PLIC advection to MOF advection. None of the above methods guarantee both mass conservation and free stream preserving for all scenarios. We investigate the geometrical error, mass error and order of accuracy with several 2D and 3D tests. Besides, we also proposed a simple and efficient algorithm that calculates the volume fractions and centroids of the linear interface analytically. This paper is organized as follows: Section 2 shows the governing equations; Section 3 reviews the MOF reconstruction; The implementation of the above-mentioned MOF advection schemes are introduced in Section 4; Section 5 shows the geometrical algorithms for the linear interface; Several 2D and 3D numerical tests are investigated in Section 6; Conclusions are drawn in Section 7.

Note that the all results are based on the author's implementation, The source code and test cases are available on <https://github.com/zhoutengye/NNMOF>.

2. Governing Equations

In MOF method, the characteristic function (or color function) c is used to indicates the fluid type

$$c(\mathbf{x}) = \begin{cases} 1 & \text{if } \mathbf{x} \in \text{fluid phase} \\ 0 & \text{if } \mathbf{x} \in \text{other phases} \end{cases}. \quad (1)$$

The volume fraction C is a discretized version of the color function. As an extension of the VOF-PLIC method, the volume fraction is defined follows that in VOF method

$$C = \frac{\int_{\Omega} c(\mathbf{x})dV}{\int_{\Omega} dV}, \quad (2)$$

with the corresponding centroid defined from the first moment of the characteristic function

$$\mathbf{x}_c = \frac{\int_{\Omega} \mathbf{x}c(\mathbf{x})dV}{\int_{\Omega} c(\mathbf{x})dV}, \quad (3)$$

where Ω is the domain of the discretized grid cell. Giving a velocity field \mathbf{u} , a standard advection equation governs the evolution of volume fraction C and the centroid \mathbf{x}_c

$$\frac{dC}{dt} = 0 \rightarrow \frac{\partial C}{\partial t} + \mathbf{u} \cdot \nabla C = 0, \quad (4)$$

$$\frac{d\mathbf{x}_c}{dt} = \mathbf{u}. \quad (5)$$

For incompressible flow, Eq. (4) can be recast in conservation form

$$\frac{\partial C}{\partial t} + \nabla \cdot (C\mathbf{u}) = 0. \quad (6)$$

However, in numerical discretization, the velocity field may not always divergence-free, especially for some multi-step schemes. Eq. (6) is typically solved with a divergence correction term

$$\frac{\partial C}{\partial t} + \nabla \cdot (C\mathbf{u}) = C\nabla \cdot \mathbf{u}. \quad (7)$$

Rider and Kothe [22] show that even for incompressible flow, the divergence correction term in Eq. (7) help improving the local and global mass conservation. In this study, our algorithms are based on the divergence correction form.

The MOF method contains two key steps: (1) reconstruction algorithm (2) advection algorithm. The reconstruction algorithm approximates the material in cell as a cut-off polyhedron (or cut-off polygon in 2D) from the computational grid cell, the volume fraction and centroid of the cut-off in Eq. (2) is determined from the cut-off polyhedron (polygon). The advection algorithm solves Eq. (5) and Eq. (7), with the known information at step n and advance to time step $n + 1$. Several important conditions should always satisfy for incompressible flow:

1. Global conservation condition

For incompressible flow, the global mass should always conserve.

$$\int_{\Omega_g} C^n dV = \int_{\Omega_g} C^{n+1} dV, \quad (8)$$

2. Local bound condition

No overshooting or undershooting for volume fraction, which means no volume fraction smaller than the empty cell or greater than a full cell. In addition, the centroid should always be located within the grid cell Ω

$$\begin{aligned} 0 \leq C \leq 1 \\ \mathbf{x}_c \in \Omega \end{aligned} \quad (9)$$

3. Global geometrical consistency condition during an advection step, the sum of the pre-image or post-image should remain consistency, which means no hole or overlap should happen.

The above 3 conditions are usually not be satisfied simultaneously. For split advection method, even for a divergence-free velocity field, the velocity field in each of the sub-step is not necessarily divergence free. This may bring in additional bound violation for volume fraction and the centroid. the volume fraction is forced to be revalued to ϵ or $1 - \epsilon$, and the centroid is forced be revalued to $(\epsilon, \epsilon, \epsilon)$ or $(0.5, 0.5, 0.5)$. Where ϵ is a very small number. In this study, $\epsilon = 1 \times 10^{-14}$. If the correction happens, the other two conditions, global conservation and global geometrical consistency are no longer hold. There are some way to enforce the global conservation or local bound conditions, but the global geometrical consistency condition is rather stringent for split advection method.

3. MOF reconstruction

The MOF method introduces the centroid as an additional constraint to determine the reconstruction interface. Unfortunately, the known centroid $\mathbf{x}_{c_{ref}}$ and volume fraction C_{ref} may not simultaneously satisfy with a linear cut-off. The exact centroid matching is sacrificed on the altar of volume conservation. A linear cut-off with the given volume fraction which provides the best approximation to the reference centroid is used as the optimized cut-off for MOF method.

The MOF method reconstructs the interface in a 3D rectangular hexahedron cell with a plane

$$\{\mathbf{x} \in \mathbb{R}^3 \mid \mathbf{n} \cdot (\mathbf{x} - \mathbf{x}_0) + \alpha = 0\}, \quad (10)$$

where \mathbf{n} is the normal vector, \mathbf{x}_0 is reference point of the cell, either the center of the cell or the lower corner of the cell, depending on the computational algorithm. b is the parameter that represents the distances from the reference point \mathbf{x}_0 . the volume of the cutting polyhedron by the reconstruction plane satisfies

$$|C_{\text{ref}} - C_A(\mathbf{n}, b)| = 0, \quad (11)$$

where C_{ref} indicates the volume of the cutting polyhedron and C_A indicates the actual volume. In addition to the the constraint on volume fraction, the MOF reconstruction also minimizes error between the reference centroid $\mathbf{x}_{\text{c}_{\text{ref}}}$ and the actual centroid \mathbf{x}_{c_A} (See Fig. 1)

$$E_{\text{MOF}} = \|\mathbf{x}_{\text{c}_{\text{ref}}} - \mathbf{x}_{\text{c}_A}(\mathbf{n}, b)\|_2. \quad (12)$$

In 3D, Eq. (12) has 4 parameters. As b can be determined by the flood algorithm and the normal vector can be parameterized with

$$\mathbf{n} = \begin{pmatrix} \sin(\phi) \cos(\theta) \\ \sin(\phi) \sin(\theta) \\ \cos(\phi) \end{pmatrix}, \quad (13)$$

Eq. (12) is simplified as a function of ϕ and θ .

$$E_{\text{MOF}}(\phi^*, \theta^*) = \|\mathbf{f}(\phi^*, \theta^*)\|_2 = \min_{(\phi, \theta): \text{Eq. (11) holds}} \|\mathbf{f}(\phi, \theta)\|_2, \quad (14)$$

where,

$$\mathbf{f} : \mathbb{R}^2 \rightarrow \mathbb{R}^3, \quad \mathbf{f}(\phi, \theta) = (\mathbf{x}_{\text{ref}} - \mathbf{x}_A(\phi, \theta)). \quad (15)$$

The minimization problem in Eq. (14) is a non-linear least square problem for ϕ and θ , which is solved numerically with optimization algorithm. Note that the expression for 2D problem is similar.

In the original MOF method [7], the non-linear optimization Eq. (14) is solved with Broyden-Fletcher-Goldfarb-Shanno (BFGS) algorithm. Several improvements has been done to accelerate the MOF reconstruction, more specifically, on the geometrical algorithm to find the centroid during iteration [13, 15]. Lemoine et al. [14] proposed an analytic algorithm that calculates the optimized centroid directly, without any numerical iteration. Unfortunately, this algorithm cannot be extended to 3D.

In this study, the analytic approach of Lemoine et al. [14] is used for 2D reconstruction, and the numerical approach of Milcent and Lemoine [15] is used for 3D reconstruction.

4. MOF advection

Similar to VOF-PLIC method, the advection of volume fraction and centroid in MOF method can be solved either with unsplit scheme [7] and directional splitting scheme [9, 18]. In either scheme, the advection procedure is

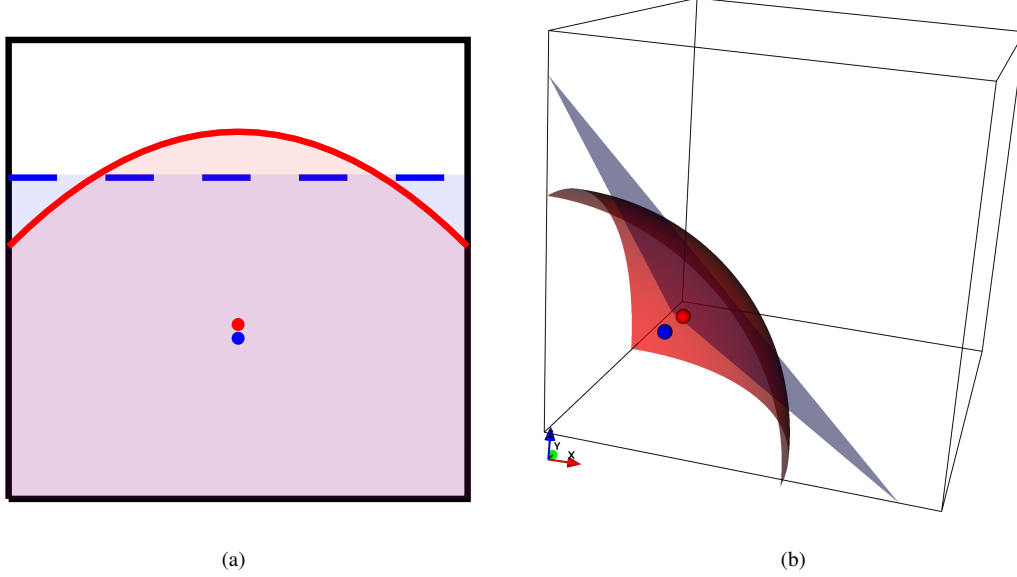


Figure 1: (a) 2D view and (b) 3D view of the MOF reconstruction. The red curve (surface) is the true interface and the blue line (surface) is the reconstructed interface by MOF. The centroid of the reconstruct interface (blue dot) is the optimized centroid that minimized the distance between the reconstructed centroid and the reference centroid (red dot) with same volume fraction.

performed as mapping the fluid from the departure region to the target region. By finding the intersection between the fluid and the target region, the volume fraction and centroids at new time step are determined. It is important to guarantee the centroid associated to its phase packet during advection. By using the fact that the material centroids in the incompressible flow move similarly to Lagrangian particles (See proof in [19] Appendix A), the consistency between Eq. (5) and Eq. (7) are guaranteed. In this paper, we use directional splitting method for advection. In rectangular hexahedron grid, the sub-regions in the departure region and target regions are rectangular hexahedron.

Eq. (7) is typically discretized with multi-step operator splitting algorithm, a typical discretization in $x - y - z$ coordinate contains three swppes:

$$\begin{aligned}
 C_{i,j,k}^{(1)} &= C_{i,j,k}^n + (F_{i-1/2}^u - F_{i+1/2}^u) + C_{i,j,k}^{<1>} (u_{i+1/2} - u_{i-1/2}), \\
 C_{i,j,k}^{(2)} &= C_{i,j,k}^{(1)} + (F_{j-1/2}^v - F_{j+1/2}^v) + C_{i,j,k}^{<2>} (v_{j+1/2} - v_{j-1/2}), \\
 C_{i,j,k}^{n+1} &= C_{i,j,k}^{(2)} + (F_{k-1/2}^w - F_{k+1/2}^w) + C_{i,j,k}^{<3>} (w_{k+1/2} - w_{k-1/2}).
 \end{aligned} \tag{16}$$

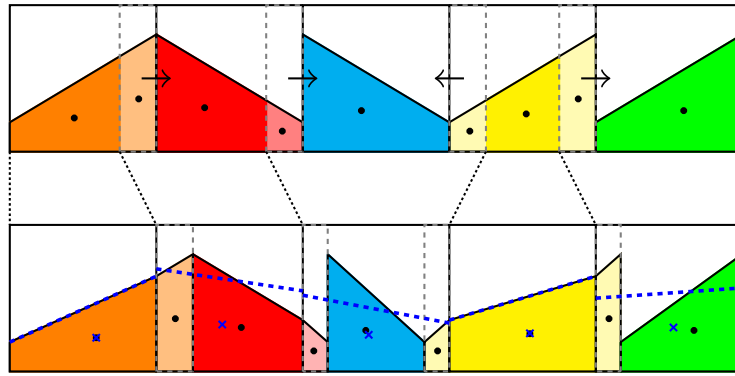
Where $C_{i,j,k}^{(1)}$ and $C_{i,j,k}^{(2)}$ are the volume fraction at the intermediate step. F is the flux, will be determined either in an Lagrangian or Eulerian approach. $C^{<>}$ means the volume function used for divergence correction, the value is determined based on the advection scheme. Note that the sequence of the sweep could change based on the implementation. The volume fraction and flux in Eq. (16) are determined from the intersection of the fluid and the target region, the centroid of the corresponding intersection can be determined using the scheme in the previous section. In

every directional split advection, the new centroid can be calculated by weighted averaging

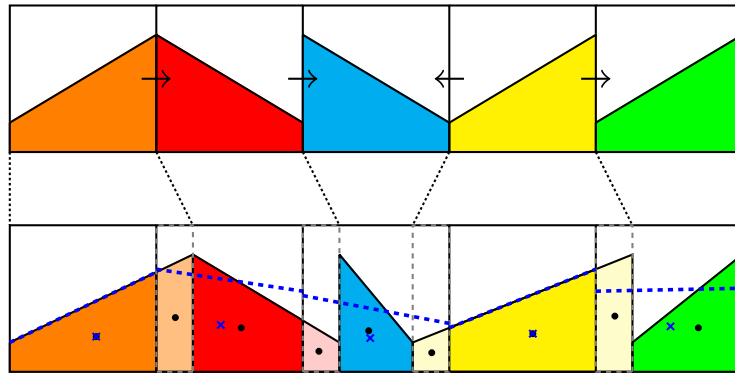
$$\mathbf{x}_c = \mathcal{M} \left(\frac{\sum V_i \mathbf{x}_i}{\sum V_i} \right), \quad (17)$$

where i indicates the sub-region in the target region and V_i indicates the volume fraction C or F in Eq. (16). \mathcal{M} is the mapping form for the centroid, which is based on the implementation of the advection scheme.

4.1. Eulerian implicit scheme



(a) Eulerian implicit (EI) advection



(b) Lagrangian explicit (LE) advection

Figure 2: The Eulerian implicit scheme (EI) and Lagrangian Explicit (LE) scheme for advection of volume fraction and centroids from step n to step $*$. The mapping procedure is indicated by the black dotted line and the gray dashed line indicates the flux region. The new volume fraction at time $*$ are determined by the summation of smaller pieces of polyhedrons. The new reconstruction interface and centroid are plotted with blue dashed line and blue cross, respectively.

The basic features for Eulerian implicit advection is plotted in Fig. 2 (a). For simplicity and clarity, we assume the z -component of the normal vector $n_z = 0$, so that the reconstructed polyhedron can be mapped to the $x - y$ plane as a 2D view. We also assume the same velocity magnitude in all cell faces and the two boundary velocity equals to 0. The 5 mappings from n to $n + 1$ in Fig. 2 corresponds with one-way expansion, linear translation, two-way compression, two-way expansion and one-way compression.

The key steps in Eulerian implicit advection scheme in x direction are:

- Determine the departure region and its sub-regions.

By employing the upwinding $y - z$ plane (2D view in Fig. 2 vertical line), every cell region Ω_i^n is now divided into smaller sub-regions. In directional splitting Eulerian implicit scheme, the mapping from the departure region to the target region of grid cell i is defined as

$$\Omega_{i,\text{depart}}^n \rightarrow \Omega_{i,\text{target}}^{n+1} = \{x_{i-1/2} - u_{i-1/2}\Delta t, x_{i+1/2} - u_{i+1/2}\Delta t\} \rightarrow \{x_{i-1/2}, x_{i+1/2}\}. \quad (18)$$

The departure region Ω_i^n can be expressed as the union of two flux regions and one center region

$$\Omega_{i,\text{depart}}^n = \Omega_{i,\text{center}}^n \cup \Omega_{i-1/2,\text{flux}}^n \cup \Omega_{i+1/2,\text{flux}}^n, \quad (19)$$

where,

$$\Omega_{i,\text{center}} = [\max(x_{i-1/2}, x_{i-1/2} - u_{i-1/2}\Delta t), \min(x_{i+1/2}, x_{i+1/2} + u_{i+1/2}\Delta t)], \quad (20)$$

$$\begin{aligned} \Omega_{i+1/2,\text{flux}} &= \Omega_{i+1,\text{target}}^n \cap \Omega_{i,\text{depart}}^n \\ &= \begin{cases} [x_{i+1/2}, x_{i+1/2} + u_{i+1/2}\Delta t], & \text{if } u_{i+1/2} > 0 \\ \emptyset, & \text{if } u_{i+1/2} < 0 \end{cases}, \end{aligned} \quad (21)$$

$$\begin{aligned} \Omega_{i-1/2,\text{flux}} &= \Omega_{i-1,\text{target}}^n \cap \Omega_{i,\text{depart}}^n \\ &= \begin{cases} [x_{i-1/2} - u_{i-1/2}\Delta t, x_{i-1/2}], & \text{if } u_{i-1/2} > 0 \\ \emptyset, & \text{if } u_{i-1/2} < 0 \end{cases}. \end{aligned} \quad (22)$$

- Find the volume fraction and the centroid of each sub-region using the reconstruction algorithm in the previous section.
- Mapping the volume fraction and the centroid from the departure region to the target region

We define the mapping ratio in Eulerian implicit scheme as

$$\beta = \frac{1}{1 + u_{i-1/2}\Delta t/\Delta x - u_{i+1/2}\Delta t/\Delta x}. \quad (23)$$

The value of β indicates

$$\begin{cases} \beta < 1, & \text{compression} \\ \beta = 1, & \text{translation} \\ \beta > 1, & \text{expansion} \end{cases}. \quad (24)$$

The new volume fraction and centroids can be calculated with

$$C_i^* = \beta (V_{i,\text{center}}^n + V_{i-1/2,\text{flux}}^n + V_{i+1/2,\text{flux}}^n), \quad (25)$$

$$\mathbf{x}_{\mathbf{c}_i}^* = \beta \frac{\mathbf{x}_{\mathbf{c}_{i,\text{center}}}^n V_{i,\text{center}}^n + \mathbf{x}_{\mathbf{c}_{i-1/2,\text{flux}}}^n V_{i-1/2,\text{flux}}^n + \mathbf{x}_{\mathbf{c}_{i+1/2,\text{flux}}}^n V_{i+1/2,\text{flux}}^n}{C_i^*} - \mathbf{x}_0, \quad (26)$$

where $\mathbf{x}_0 = (x_i - 1/2, y_j, z_k)$.

Eq. (25) is equivalent to Eq. (16) when the divergence correction term in $C^{<1>_{i,j,k}} = C^n_{i,j,k}$ in Eq. (16). The EI mapping ensures all polyhedron in sub-regions aligned to the cell, thus no overshooting or undershooting will happen, the corresponding centroid is confined within the grid region, thus the local bound condition holds during every split EI advection step.

4.2. Lagrangian Explicit scheme

The mapping strategy in Lagrangian Explicit scheme (LE) is slightly different from the EI scheme. The departure region in LE scheme is Ω_i^n and the target region are determined by the downwinding $y - z$ plane (2D view in Fig. 2 vertical line). In LE scheme, the flux are calculated after mapping. The key steps in LE advection are:

- Determine the target region and its sub-regions

In directional splitting LE scheme, the mapping from the departure region to the target region of grid cell i is defined as

$$\Omega_{i,\text{depart}}^n \rightarrow \Omega_{i,\text{target}}^{n+1} = \{x_{i-1/2}, x_{i+1/2}\} \rightarrow \{x_{i-1/2} + u_{i-1/2}\Delta t, x_{i+1/2} + u_{i+1/2}\Delta t\}. \quad (27)$$

The target region Ω_i^{n+1} can be expressed as the union of two flux regions and one center region

$$\Omega_{i,\text{target}}^{n+1} = \Omega_{i,\text{center}}^{n+1} \cup \Omega_{i-1/2,\text{flux}}^{n+1} \cup \Omega_{i+1/2,\text{flux}}^{n+1}, \quad (28)$$

where,

$$\Omega_{i,\text{center}}^{n+1} = [\min(x_{i-1/2}, x_{i-1/2} + u_{i-1/2}\Delta t), \max(x_{i+1/2}, x_{i+1/2} + u_{i+1/2}\Delta t)], \quad (29)$$

$$\begin{aligned} \Omega_{i+1/2,\text{flux}}^{n+1} &= \Omega_{i+1,\text{depart}}^n \cap \Omega_{i,\text{target}}^{n+1} \\ &= \begin{cases} [x_{i+1/2}, x_{i+1/2} + u_{i+1/2}\Delta t], & \text{if } u_{i+1/2} > 0 \\ \emptyset, & \text{if } u_{i+1/2} < 0 \end{cases}, \end{aligned} \quad (30)$$

$$\begin{aligned} \Omega_{i-1/2,\text{flux}}^{n+1} &= \Omega_{i-1,\text{depart}}^n \cap \Omega_{i,\text{target}}^{n+1} \\ &= \begin{cases} [x_{i-1/2} + u_{i-1/2}\Delta t, x_{i-1/2}], & \text{if } u_{i-1/2} > 0 \\ \emptyset, & \text{if } u_{i-1/2} < 0 \end{cases}. \end{aligned} \quad (31)$$

- Mapping the volume fraction and the centroid from the departure region to the target region.

In LE scheme, The flux is not determined from the departure region, but is estimated from the intersection of remapped polyhedron and the target region and the grid cells. The mapping factor in LE advection is defined as

$$\gamma = 1 - u_{i-1/2}\Delta t/\Delta x + u_{i+1/2}\Delta t/\Delta x. \quad (32)$$

Similar to the expansion factor for the EI advection in Eq. (23), the value of γ indicates

$$\begin{cases} \gamma < 1, & \text{compression} \\ \gamma = 1, & \text{translation} \\ \gamma > 1, & \text{expansion} \end{cases}. \quad (33)$$

After mapping, the normal vector of the reconstruction plane changes, the new normal vector can be determined by altering the value (α, m_x) with

$$\begin{aligned} m'_x &= \gamma m_x, \\ \alpha' &= \alpha + m_x u \Delta t / \Delta x. \end{aligned} \quad (34)$$

- Calculate the flux and center region and update volume fraction and centroids

The new volume fraction and centroid in the sub-regions can be determined by using the algorithm in previous section. The volume fraction and centroids in Ω_i^{n+1} can be determined by

The new volume fraction and volume fraction are mapped from the

$$C^* = (V_{i,\text{center}}^n + V_{i-1/2,\text{flux}}^n + V_{i+1/2,\text{flux}}^n), \quad (35)$$

$$\mathbf{x}_{\mathbf{c}}^* = \frac{\mathbf{x}_{\mathbf{c}_{i,\text{center}}}^n V_{i,\text{center}}^n + \mathbf{x}_{\mathbf{c}_{i-1/2,\text{flux}}}^n V_{i-1/2,\text{flux}}^n + \mathbf{x}_{\mathbf{c}_{i+1/2,\text{flux}}}^n V_{i+1/2,\text{flux}}^n}{C_i^*}. \quad (36)$$

The implementation of LE scheme is simple. Although the the LE advection can be expressed as a mapping procedure (See Fig. 2), the mapping procedure does not have to be solved explicitly. Simply by altering the slope the α , the sub-regions in Ω^{n+1} are determined. When the divergence correction term in $C^{<1>_{i,j,k}} = C_{i,j,k}^n$ in Eq. (16), the expression is equivalent to Eq. 35. LE advection also automatically takes the divergence term into account. Same as EI advection, a single split LE advection satisfies the local bound condition for both volume fraction and centroid.

4.3. EI-LE strategy in 2D

Scardovelli and Zaleski [20] show that both EI and LE operator splitting advection schemes satisfies the local bound condition, neither of them guarantees the global mass conservation if only one of them is used. The main reason that causes the unconserved mass is the overlap or "hole" of between the departure and arrival regions between two time steps, which consists of multiple split advections. The global geometrical consistency condition will not hold as well, which brings in additional error to the advection of centroid. A hybrid EI-LE scheme [20, 1] (in this paper, referred to as EILE2D) is proposed which ultimately conserves volume. Assume the operator splitting advection starts with an EI advection in x -direction and subsequently applies an LE advection y -direction (See Fig. 3 (a)), the two mapping steps are

$$\begin{aligned} \Pi_x = \Omega_{\text{depart}} \rightarrow \Omega_{i,j} &= \begin{cases} x = \beta_x (x' + u_1) \\ y = y' \end{cases}, \\ \Pi_y = \Omega_{i,j}^n \rightarrow \Omega_{\text{target}} &= \begin{cases} x'' = x \\ y'' = \gamma_y y + v_1 \end{cases}, \end{aligned} \quad (37)$$

where,

$$\beta_x = \frac{1}{1 + u_1 - u_2}, \quad (38)$$

$$\gamma_y = 1 - v_1 + v_2.$$

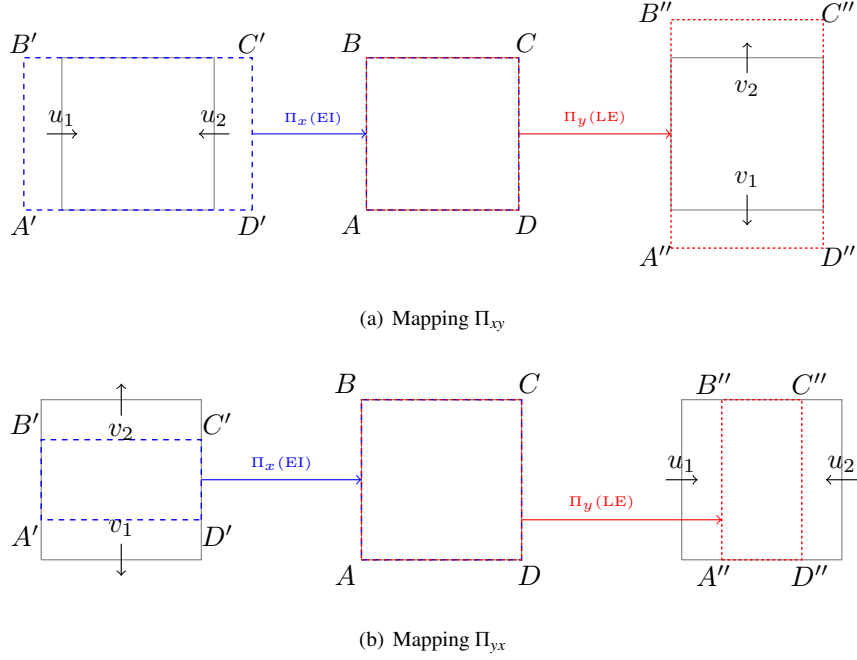


Figure 3: Mapping from the departure region Ω_{depart} to the target region Ω_{target} during EILE2D advection. (a) Mapping Π_{xy} starts with EI advection in x direction then LE advection in y direction. (b) Mapping Π_{yx} starts with EI advection in y direction and then LE advection in x direction.

The mapping from the departure region and target region Π_{xy} can be expressed as

$$\Pi_{xy} = \Pi_x \Pi_y = \begin{cases} x'' = \beta_x (x' + u_1) \\ y'' = \gamma_y y' + v_1 \end{cases}. \quad (39)$$

With the divergence-free constraint

$$u_2 - u_1 = v_1 - v_2. \quad (40)$$

The Jacobian of the transformation $J = \beta_x \gamma_y = 1$. This transformation is an volume-preserving mapping. When the advection starts with y -direction, the EI-LE scheme also guarantees volume-preserving (See Fig. 3 (b)), thus condition Eq. (9) satisfies. Since both EI and LE advection are consistent with condition Eq. (8), the EI-LE scheme satisfied both of the conditions required by VOF. Note that the mapping factors in Eq. (39) are consistent with the mapping factors in Eq. (23) and Eq. (32), the volume-preserving also guarantees the correct mapping of the centroid during MOF advection. If the sweep is done with a reversed order, which starts with an LE advection and then an EI advection (referred to as LEEI2D), none of global conservation or global geometrical consistency condition will hold.

4.4. EI-LE strategy in 3D

Unfortunately, the EILE strategy cannot extend to 3D directly. Aulisa et al. [1] show that the ultimate geometrical preserving in 3D can be achieved by decomposing the velocity field to three 2D divergence-free velocity fields

$\mathbf{u}_1 = (\bar{u}_1, \bar{v}_1, 0)$, $\mathbf{u}_2 = (\bar{u}_2, 0, \bar{w}_2)$, $\mathbf{u}_3 = (0, \bar{v}_3, \bar{w}_3)$ which satisfied

$$\begin{aligned}\mathbf{u} &= \mathbf{u}_1 + \mathbf{u}_2 + \mathbf{u}_3, \\ \nabla \cdot \mathbf{u}_1 &= 0, \\ \nabla \cdot \mathbf{u}_2 &= 0, \\ \nabla \cdot \mathbf{u}_3 &= 0.\end{aligned}\tag{41}$$

One simple approach to composite the 3D velocity field is to use the fact that the only 5 of the 6 unknowns $(\bar{u}_1, \bar{u}_2, \bar{v}_1, \bar{v}_2, \bar{w}_1, \bar{w}_2)$ are independent. By set $\bar{u}_1 = u/2$ for the whole domain, and the lower boundary value of $\bar{v}_{1,i,j-1/2,k} = v_{i,j-1/2,k}/2$, solve for $\bar{v}_{1,i,j+1/2,k}$ using the relationship $\nabla \cdot \mathbf{u}_1 = 0$. The other components can be solved recursively by using other divergence-free constraints. Although the decomposition starts with a halved velocity component, the velocity decomposition may not guarantee the magnitude of the velocity bounded to the maximum magnitude of the original velocity field. An example of unbounded decomposition is shown in Section 6.2.2.

A simplified EI-LE strategy in 3D (EILE3DS) is to alter the EI and LE sweeps in two time steps. For odd step, the sweep is X(EI)-Y(LE)-Z(EI); while for even step, sweep is X(LE)-Y(EI)-Z(LE) [23]. This approach does not guarantee volume preserving, however, improved the mass conservation of pure EI or LE advection. Note that the strategy Aulisa et al. [24] also named EILE3DS, however, implemented with 6 split advection for a full time step, which is different implementation from this study.

4.5. EI-EA-LE strategy in 3D

In this study, we proposed a simplified EI-LE splitting scheme for both centroid and volume fraction. Baraldi et al. [26] introduced an EA (Eulerian algebraic) step between the EI and LE advection. The mapping at EA step is determined by enforcing the Jacobian $J = 1$ for the mapping $\Pi_{xyz} = \Omega_{\text{depart}} \rightarrow \Omega_{\text{target}}$, which does not have a geometrical interpretation. With the approximate intermediate step, the mass conservation is significantly improved compared with EI or LE advection. In the numerical test of Baraldi et al. [26], the mass conservation reaches machine precision with their wisp-suppression algorithm. In this study, we use a similar approach for both volume fraction and centroid advection, without wisp-suppression algorithm.

The advection consists of three steps. Consider the mapping Π_{xyz} corresponds with the sweep sequence of $x-y-z$, the mapping during the advection from n to $n+1$ is

$$\Pi_{xyz} = \Omega_{\text{depart}} \rightarrow \Omega_{\text{target}} = \begin{cases} x = \beta_x(x' + u_1) \\ y = \xi_{y1}(\xi_{y2}y' + v_1) \\ z = \gamma_z z' + w_1 \end{cases}\tag{42}$$

The expression of β_x and γ_z are consistent with Eq. (38) in EILE2D scheme. The intermediate step is an algebraic step, to ensure that the Jacobian $\beta_x \xi_{y1} \xi_{y2} \gamma_z$ equal to 1, ξ_{y1} and ξ_{y2} are expressed as

$$\xi_{y1} = \frac{1}{\gamma_z}, \quad \xi_{y2} = \frac{1}{\beta_x}.\tag{43}$$

For split advection procedure, the mapping Eq. (42) is implemented with

$$\begin{aligned}\Pi_x &= \Omega_{\text{depart}_1} \rightarrow \Omega_{\text{target}_1} = x = \beta_x (x' + u_1), \\ \Pi_y &= \Omega_{\text{depart}_2} \rightarrow \Omega_{\text{target}_2} = y = \xi_{y1} (\xi_{y2} y' + v_1), \\ \Pi_z &= \Omega_{\text{depart}_3} \rightarrow \Omega_{\text{target}_3} = z = \gamma_z z' + w_1.\end{aligned}\tag{44}$$

Because of the non-geometrical property of the intermediate EA step, $\Omega_{\text{target}_1} \neq \Omega_{\text{depart}_2}$ and $\Omega_{\text{target}_2} \neq \Omega_{\text{depart}_3}$, the mapping $\Pi_{xyz} \neq \Pi_x \Pi_y \Pi_z$. Although the Jacobian of Π_{xyz} equals to 1, the Jacobian of $\Pi_x \Pi_y \Pi_z$ would not always equal to 1.

The expression of the volume fraction and centroid of the x sweep and z sweep corresponds with the expression in EI and LE advection, respectively. The volume fraction in EA step are calculated with

$$C_{i,j,k}^{(2)} = \frac{C_{i,j,k}^{(1)} (1 - \delta_x \bar{u}) + F_{j-1}^v - F_j^v}{1 + \delta_z \bar{w}}.\tag{45}$$

For the centroid, since there is no corresponding geometrical mapping for the EA step, the centroid is calculated with the EI method as in Eq. (26).

We have not found any proof that the EA step satisfies the local bound condition due to the non-geometrical property. Numerical test show that EIEILA scheme would not guarantee the ultimate mass conservation.

4.6. WY approach

The strategy by Weymouth and Yue [25] can be categorized as an EI advection, as the flux calculation follows the EI approach. The flux correction term $C^{<>}$ in Eq. (16) is applied based on the value of the volume fraction at step n

$$C_{i,j,k}^{<1>}(u_{i+1/2} - u_{i-1/2}) = \tilde{C}_{i,j,k} = \begin{cases} 0, & C_{i,j,k}^n \geq \frac{1}{2} \\ 1, & C_{i,j,k}^n < \frac{1}{2} \end{cases}.\tag{46}$$

The correction does not rely on the velocity field, but is only based on the volume fraction at time step n . Weymouth and Yue [25] prove that with the threshold $1/2$, there is no over shooting or undershooting for the volume fraction, and ultimately mass preserving. However, the flux correct term is an algebraic correction, there is no corresponding geometrical expression. There is no corresponding form for the correction in Eq. (46) for the centroid. The EI centroid advection is applied along with the WY volume correction in Li et al. [23]. In this study, we use the same strategy to the centroid. The EI advection of the centroid guarantees the centroid in the grid cell. With the volume fraction bounded between 0 and 1, the local bound condition of MOF advection holds. Due to the non-geometrical correction, the global geometrical consistency condition does not hold for WY approach.

4.7. Summarize

Among all fluxed-splitting MOF advection methods mentioned in this section, the key idea is to manipulate the divergence correction term, either by changing the mapping strategy or apply modification to correction term directly. The 2D and 3D methods are summarized in Table 1 and Table 2.

Table 1: Summary of 2D advection methods, where P_1 indicates the global mass conservation condition, P_2 indicates the local bound condition, P_3 indicates the global geometrical consistency condition, n_s is the split advection sweep per full advection step.

Method	P_1	P_2	P_3	n_s	CFL limit
EI	×	○	×	2	1/2
LE	×	○	×	2	1/2
EILE2D	○	○	○	2	1/2
LEEI2D	×	○	×	2	1/2
WY	○	○	×	2	1/4

Table 2: Summary of 3D advection methods, where P_1 indicates the global mass conservation condition, P_2 indicates the local bound condition, P_3 indicates the global geometrical consistency condition, n_s is the split advection sweep per full advection step.

Method	P_1	P_2	P_3	n_s	CFL limit
EI	×	○	×	3	1/2
LE	×	○	×	3	1/2
EILE3D	○	○	○	6	1 (?)
EILE3DS	×	○	×	3	1/2
EI-EA-LE	×	○ (?)	×	3	1/2
WY	○	○	×	3	1/6

For 2D methods, all methods satisfies the local bounded condition, which means the mass conservation issue does not come from the correction from overshooting or undershooting, but comes from the geometrical inconsistency. EI nor LE would not conserve mass because its non-volume preserving mapping. For EILE2D method, with an LE advection coming after an EI advection, satisfies all three conditions. While the LEEI2D method, although alters between LE and EI schemes at two sub-steps, would not guarantee geometrical preserving or geometrical consistency. The WY scheme ultimately conserve mass with a more stringent CFL limit than other schemes, however, due to a lack of the divergence correction, failed on the geometrical consistency condition. All the 2D strategies takes 2 sweeps in one time step.

For 3D methods, pure EI or LE scheme involves mass conservation issue as same properties to its corresponding 2D schemes. For EILE3D scheme, if the velocity decomposition guarantees divergence-free, all three conditions hold. The CFL limit seems to be 1, as the starting values of the velocity field is a halved velocity component, however, the decomposed velocity may not be bounded to a half of the velocity field the CFL limit may not be one, or could be even much smaller than 1/2. Besides, it takes twice of the advection steps of other advection methods. The EILE3DS alters between EI and LE schemes, is shown to preserve mass better than pure EI or LE scheme [17]. For EIEALE scheme, the mapping coefficient of the EA step is determined from the Jacobian equal to 1, although would not guarantee ultimate mass conservation, helps to improve the mass conservation [26]. While WY scheme in 3D has a even more stringent CFL limit than the 2D WY scheme, keeping mass conservation within its CFL limit of 1/6. Note that all methods, the local bounded condition holds for all methods, excepts for EIEALE method. Even though the EIEALE significant improve the mass conservation from EI or LE method (See Section 6), we have not find any proof to show that the EA step guarantee the local bound condition for volume fraction and centroid.

5. Geometrical algorithm for MOF

In MOF method, two problems are typically solved by geometrical algorithm:

- (1) Intersection algorithm: Find the centroid \mathbf{x}_c and volume fraction C of the cut-off polyhedra by a known plane (or in 2D the cutting polyhedra by a line).
- (2) Flood algorithm: Find the centroid \mathbf{x}_c for the cutting plane (or line in 2D) with known normal vector \mathbf{n} and volume fraction C_{ref} .

During the MOF reconstruction, the flood algorithm is typically used to determine the equation of the plane (line) and the corresponding centroid of the cutting polyhedron (polygon) with the normal vector in the current step. The MOF advection, in which is equation of the plane (line) is known, the intersection algorithm is used to determine the volume fraction and centroid in departure and target regions. Note that most of the flood algorithms contains the intersection algorithm as a part of it.

Many polyhedron (polygon) algorithms/tools have been developed for the intersection and flood algorithms for VOF-PLIC method or MOF method [27, 28, 22, 29, 30, 31]. Although those algorithms works for general grids, they

have to deal with the intersection and the volume/centroid calculation using a complex node/edge/face algorithm. For some simple shapes, analytic formulation can be found to accelerate the volume and centroid calculation [21, 32].

In this study, we implement very simple and efficient intersection and flood algorithms. With the fact that all cell and flux regions during reconstruction and advection are rectangular hexahedron (or rectangle), the intersection becomes much simpler. Unlike the computational geometrical approach, the operators for the vertex, edge or face does not have to be calculated explicitly. Here we only show the 3D algorithms, the implementation of the 2D algorithm is similar, but simpler.

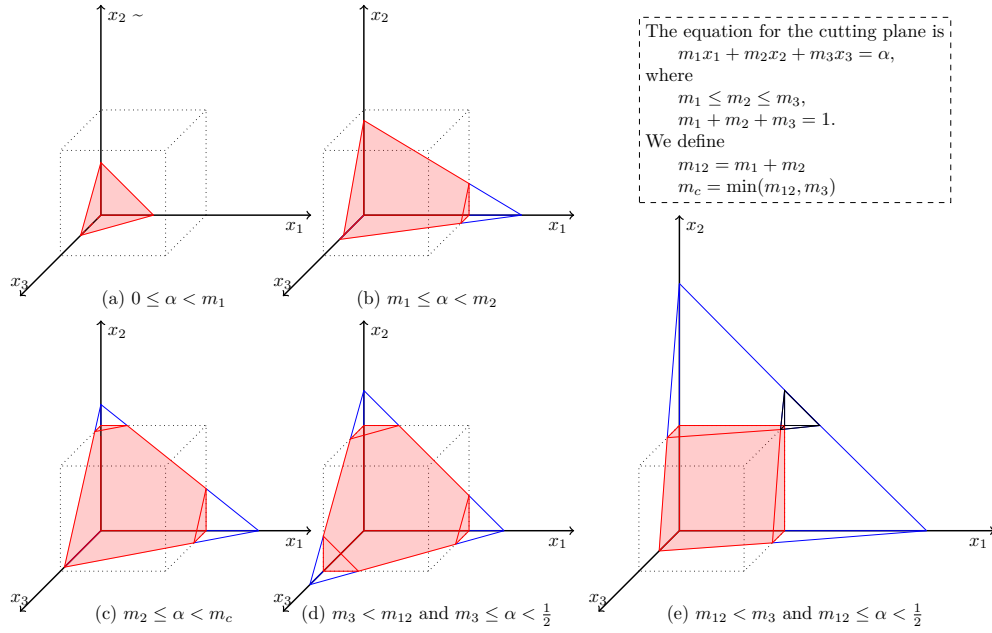


Figure 4: Five configurations of the cutting polyhedron by a plane with the intersection of (a) Triangle, (b) Quadrilateral-1, (c) Pentagon, (d) hexagon, (e) Quadrilateral-2.

The volume fraction in the intersection algorithm follows Scardovelli and Zaleski [21] which derived is derived with the combination of right tetrahedrons. By implementation symmetric, permutation and shift origin techniques, the cutting polyhedron can be simplified to 5 configurations (See Fig. 4). We derive the expression for the centroids as an extension of the approach of Scardovelli and Zaleski [21]. The volume fraction and the corresponding centroid are expressed as

$$V = \frac{1}{6m_1m_2m_3} \left[\alpha^3 - \sum_{i=1}^3 F_3(\alpha - m_i\Delta x_i) + \sum_{i=1}^3 F_3(\alpha - \alpha_{\max} + m_i\Delta x_i) \right] \quad (47)$$

$$c_j = \frac{\alpha^4}{24m_jV} \left[- \sum_{i=1}^3 (\alpha + (1 + 2\beta)m_i\Delta x_i) F_3(\alpha - m_i\Delta x_i) + \sum_{i=1}^3 (\alpha + (1 - 2\beta)(\alpha_{\max} - m_i\Delta x_i)) F_3(\alpha - \alpha_{\max} + m_i\Delta x_i) \right] \quad (48)$$

Where

$$\alpha_{\max} = \sum_{i=1}^3 m_i \Delta x_i, \quad (49)$$

$$\beta = \begin{cases} -1 & \text{for } i \neq j \\ 1 & \text{for } i = j \end{cases}, \quad (50)$$

$$F_n(y) = \begin{cases} y^n & \text{for } y > 0 \\ 0 & \text{for } y \leq 0 \end{cases}, \quad (51)$$

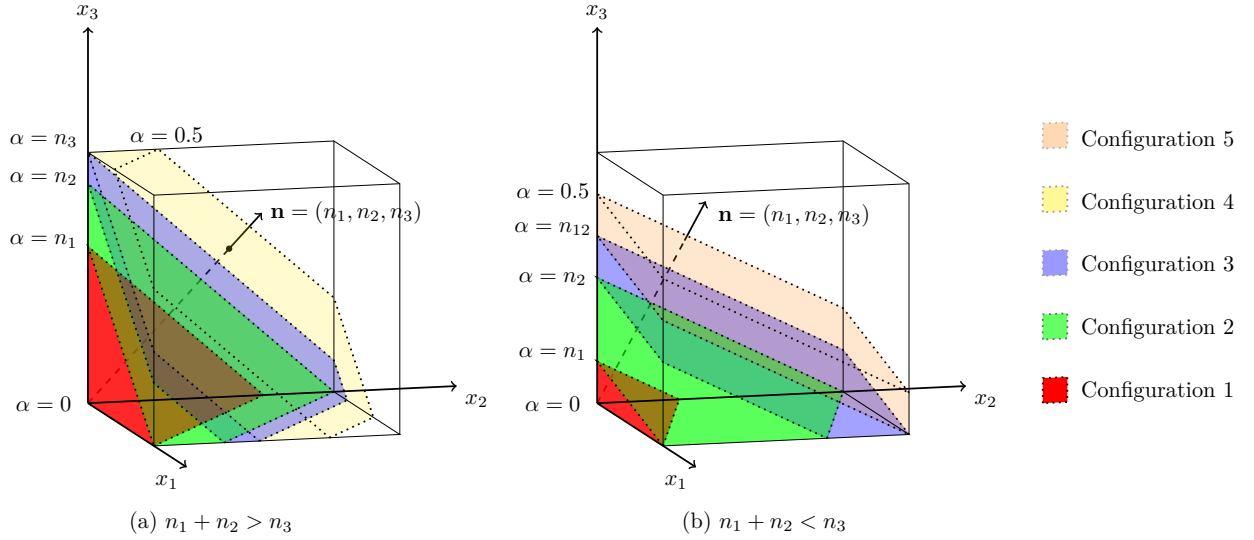


Figure 5: Flood algorithm.

Based on the values of \mathbf{n} and α , the configuration is determined from the 5 candidate cutting polyhedra and the volume fraction and centroid are calculated using a very simple and efficiency equations. The equation of the volume fraction and centroid for the 5 configurations are derived from Eq. (47) and Eq. (48). The detailed expressions are listed in Appendix A.

In flood algorithm, the parameter α can be determined directly from the inverse function of Eq. (47), the corresponding expressions for the 5 candidate configurations can be found in Scardovelli and Zaleski [21]. Although there is no explicit inverse function for Eq. (48), as the volume fraction is determined from the inverse form of Eq. (47), the centroid can now be determined from the volume fraction and the expression of the plane.

We applied both our algorithm and the geometrical algorithm of Jemison et al. [9] to the split advection methods in Section 3, on a 3D advection test (Corresponds with the Zalesak's test in Section 6.2.1). The comparison of the CPU times is shown in Fig. 3. Overall, using the same advection and reconstruction, our geometrical algorithm is about 50 times faster than the geometrical algorithm of Jemison et al. [9]. With the geometrical algorithm of Jemison et al. [9], the advection takes about 78% of the computational time during advection. While using our geometrical algorithm, the ratio of CPU time the on advection term reduces from 78% to 8%.

Table 3: CPU time on different 3D advection methods with the two geometrical algorithm for volume fraction and centroids.

Geometrical method	EI	LE	EILE3D	EILE3DS	EIEALE	WY
	47.27	47.42	123.96	45.16	50.64	51.96
Current algorithm	<i>3.95</i>	<i>3.59</i>	<i>7.93</i>	<i>3.75</i>	<i>3.94</i>	<i>4.29</i>
	0.08	0.08	0.06	0.08	0.08	0.08
	255.02	276.47	619.20	259.89	287.67	289.61
Geometrical algorithm [9]	<i>201.82</i>	<i>214.20</i>	<i>474.40</i>	<i>203.40</i>	<i>221.10</i>	<i>227.20</i>
	0.79	0.77	0.77	0.78	0.77	0.78

* The total CPU times are in normal font between mesh entries.
** The CPU times on advection term are in italics between mesh entries.
*** The ratios of advection time and total CPU time are in bold between mesh entries.

6. Numerical Tests

In this section, six typical tests are taken to evaluate the performance of different split MOF advection methods. Three of them are in 2D, and other three of the are in 3D. The candidate methods for 2D and 3D are listed in Table 1 and 2. For all the numerical tests, the reconstruction algorithm, centroid algorithm and flood algorithm are identical. For MOF reconstruction algorithm, the maximum iteration is 10, and the tolerance for iteration is 10^{-8} .

Two different error measurement criteria [5] are used in this study:

(1) Geometrical error

$$E_g = \frac{\sum |f(T) - f_{exact}|}{N^{\dim}}, \quad (52)$$

(2) Mass error

$$E_m = \frac{\sum |f(T) - f_{exact}|}{N^{\dim}}, \quad (53)$$

where $f(T)$ is the numerical results at $t = T$, f_{exact} is the exact results, N is the grid resolution in x direction, $\dim = 2$ for 2D problem and $\dim = 3$ for 3D problem. The order of the accuracy [5, 24] is defined as

$$O_h = \log_2 \left(\frac{E^{\dim} \left(\frac{1}{2h} \right)}{E_g \left(\frac{1}{h} \right)} \right) \quad (54)$$

Note that, the CFL number in the tests can be larger than the CFL limit listed in Table 1 and Table 2.

6.1. 2D tests

6.1.1. Zalesak's disk rotation test

The Zalesak's disk rotation test is firstly introduced by Zalesak [33] and used by many other studies [34, 1, 24, 5]. In Zalesak's disk rotation, the rotation velocity field is defined with the a rotation velocity field. The setup and velocity

Parameter	value
domain	$[0, 1] \times [0, 1]$
grids	$N \times N$
grid size	$h = 1/N$ $\mathbf{x}_0 = (0.5, 0.75)$
shape	$R = 0.2, h = 0.1$ $d = 0.08$
Resolution	$N \in [16, 32, 64, 128, 256]$
CFL	$c_f \in [0.01, 0.05, 0.1, 0.15, 0.2, 0.25, 0.3, 0.5]$
Time step	$k = 2c_f/N$
n_{step}	$3N/c_f$
Velocity field	
Stream function	$\psi = \frac{\omega}{T} [(x - 0.5)^2 + (y - 0.5)^2]$
Period	$T = 6$
Angular velocity	$\omega = 0.5$

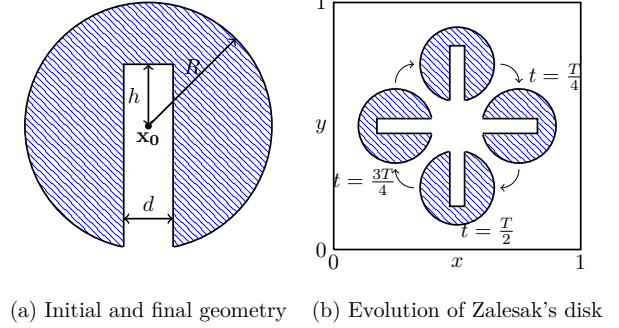


Figure 6: Initial setup and parameters of 2D Zalesak's disk rotation test

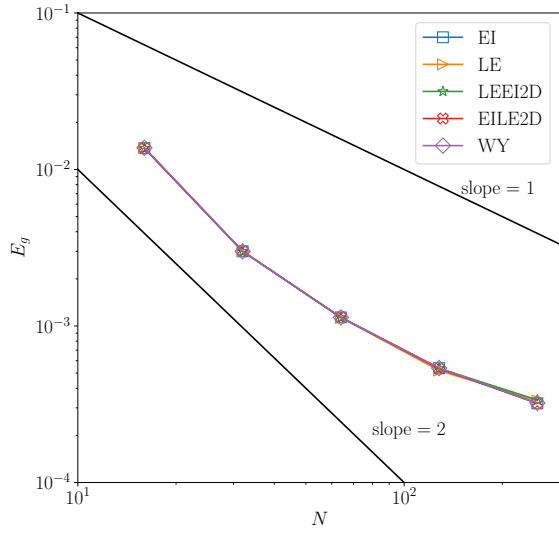
field of the Zalesak's rotation test is shown in Fig. 6. After a full revolution of 2π rotation the notched disk returns to its initial location.

The geometrical errors are shown in Fig. 7 and Fig. 8. For a fixed CFL number, the geometrical error decreases with the increase of the grid resolution. While for a fixed grid resolution, the geometrical error get larger when the CFL number becomes smaller. In this test, all methods do not show significant difference from each other when the CFL number and grid resolution N are fixed. For mass conservation, all methods conserve to machines precision with all combinations of CFL number and grid resolution N .

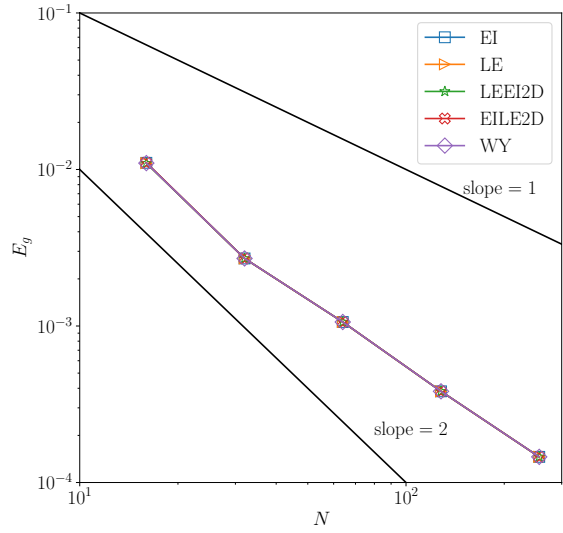
6.1.2. Rider-Kothe Single vortex test

First introduced by Rider and Kothe [22], the single vortex test represents the evolution of a circular disk under a reversed shear velocity field. The initial set up and test parameters are shown in Fig. 9. With the domain-centered vortex field, the material interface of the circular disk stretches into a filament towards the center of the vortex. The material interface reaches its maximum deformation at $t = T/2$, and recovers back to the initial circular disk at $t = T$. The material interface may get teared or smoothed out there is no sufficient numerical resolution. Note that even though the stability criteria for most of the MOF advection methods is $CFL \leq 1/2$, the CFL limit for this test could be greater than 0.5. We test $CFL = 0.8$ and $CFL = 1.0$ as well.

When the grid resolution is 64×64 , the material interfaces with different CFL number at $t = T/2$ and $t = T$ are plotted in Fig. 10. When $t = T/2$, all advection methods maintains the overall agreements with the exact resolution, with sharp corner on the tail and head smoothed out. There is no significant difference among all advection methods. When $t = T$, the material interfaces show significant difference among each other, especially when the CFL number is large. Compared with the exact circular disk, the EI and LE methods show most significant deviation. The position of the EI material interface is left of the exact result, while the position of the LE material interface right of the exact



(a) CFL= 0.05



(b) CFL= 0.5

Figure 7: Geometrical error of 2D Zalesak’s disk rotation test with repeatedly halving grid resolution at (a) CFL = 0.05 and (b) CFL = 0.5. The corresponding data is shown in Table 4.

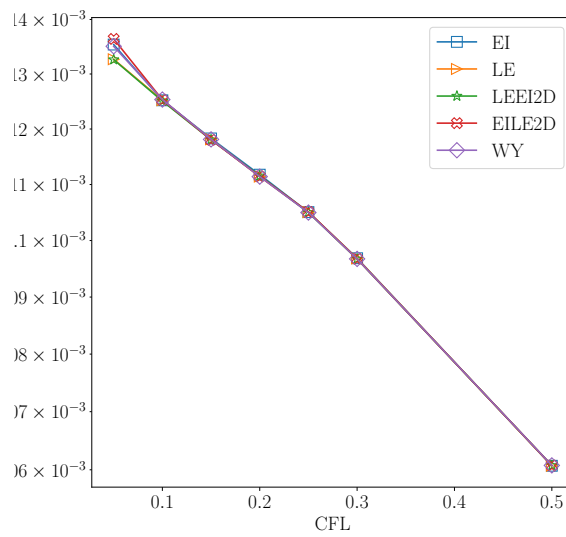
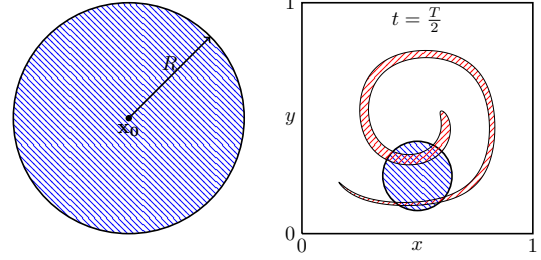


Figure 8: Geometrical error of 2D Zalesak’s disk rotation test with different CFL numbers. The corresponding data is shown in Table 5.

Parameter	value
domain	$[0, 1] \times [0, 1]$
grids	$N \times N$
grid size	$h = 1/N$
shape	$\mathbf{x}_0 = (0.25, 5)$
Resolution	$R = 0.15$
CFL	$N \in \{16, 32, 64, 128, 256\}$
Time step	$c_f \in \{0.01, 0.05, 0.1, 0.15, 0.2, 0.25, 0.3, 0.5, 0.8, 1.0\}$
n_{step}	$k = c_f/N$
	$6N/c_f$
Velocity field	
Stream function	$\psi(x, y) = \frac{1}{\pi} \sin^2(\pi x) \sin^2(\pi y) \cos\left(\frac{\pi t}{T}\right)$
Period	$T = 6$



(a) Initial and final geometry (b) Evolution of single vortex test

Figure 9: Initial setup and parameters of 2D Rider-Kothe single vortex test.

result. Other methods, although lost some accuracy at the top of the circular disk, remains close to the exact material interface.

The Geometrical error and mass conservation error with grid resolution of 64×64 are plotted in Fig. 11. The optimal CFL number that results in minimum geometrical error for each method occurs at the range of $[0.05 - 0.2]$. When CFL number is small (< 0.1), the geometrical error among all methods is not significant. After $CFL > 0.15$, with the increase of CFL number, the geometrical error increases for most of the methods. The EILE2D method and LEED2D method has overall smaller geometrical error compared with EI, LE and WY methods. For mass conservation, EILE2D method conserves mass to machine precision as expected. EI and LE has most significant mass error, especially when CFL number is large. When the CFL number is getting smaller, the mass error becomes smaller. When CFL number is 0.05, the mass error is approximately 10^{-3} . The LEEI2D method which has a reversed order of EI and LE combination to EILE2D methods, although does not satisfied the global mass conservation condition, improves the mass error compared with EI and LE methods. It is interesting to find that although the CFL number need to be smaller than $1/4$ in order to guarantee an ultimate mass preserving, the WY method preserves mass even when CFL number is 1.0 in this study.

The geometrical error and mass error with the change of grid resolution are plotted in Fig. 12. The geometrical error decreases when the grid resolution is getting larger. When CFL number is small ($CFL=0.05$ as shown in Fig. 12 (a)), the geometrical error are similar to each other for all methods. When CFL number is large ($CFL=1.0$ as shown in Fig. 12 (b)), EILE2D and LEEI2D shows a smaller geometrical error and higher order of accuracy. The EILE2D and WY methods conserves the mass to machine precision. EILE2D method improves the mass conservation compared with EI or LE method.

6.1.3. Reverse Vortex test

We introduce a even more stringent test compared with Rider-Kothe single vortex test [22]. The reverse vortex test is firstly introduced by LeVeque [35]. The initial set up and test parameters are shown in Fig. 13. The number of

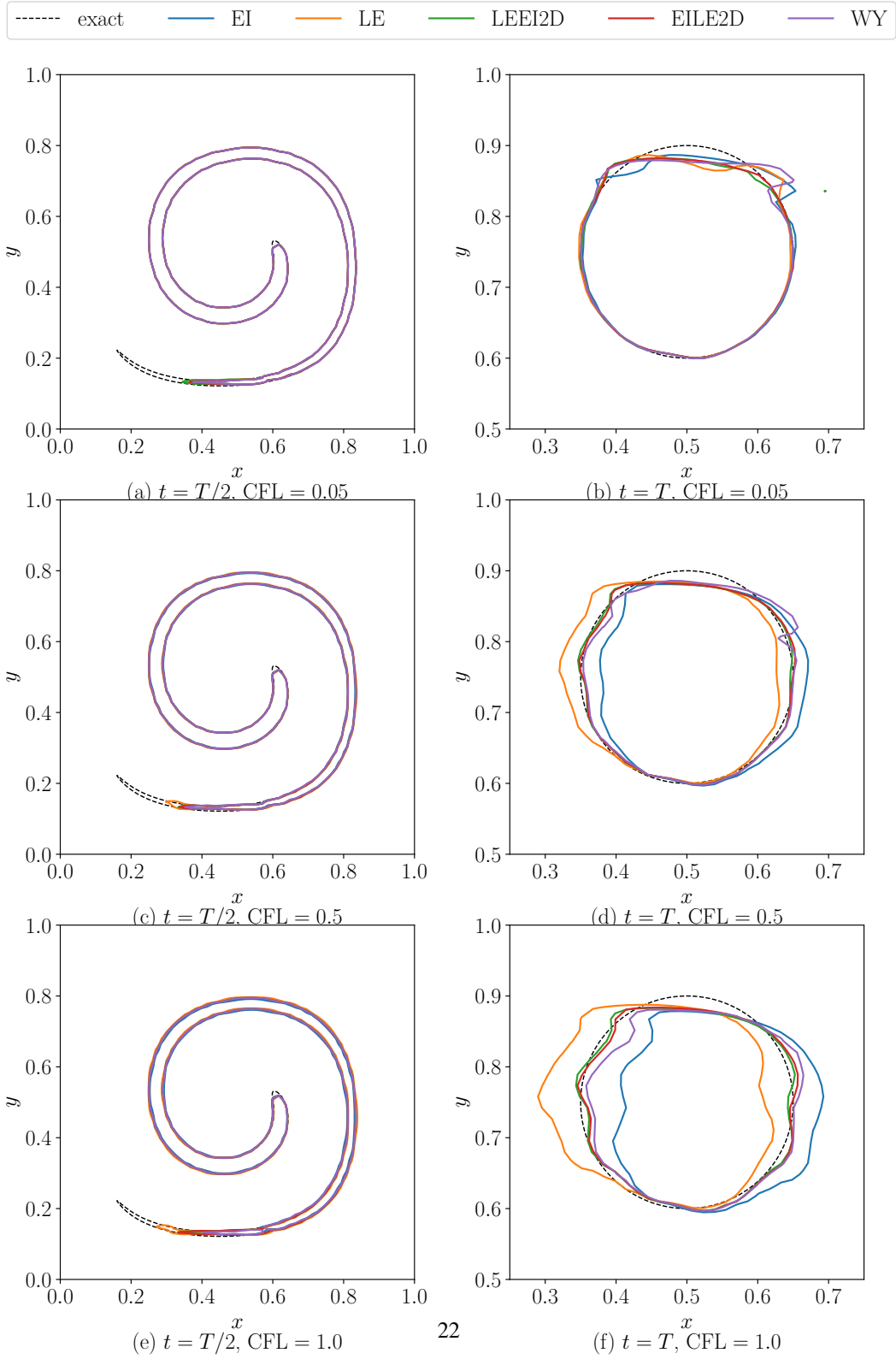


Figure 10: Material interface for 2D Rider-Kothe single vortex test represent by volume fraction $C = 0.5$ with different CFL numbers on a 64×64

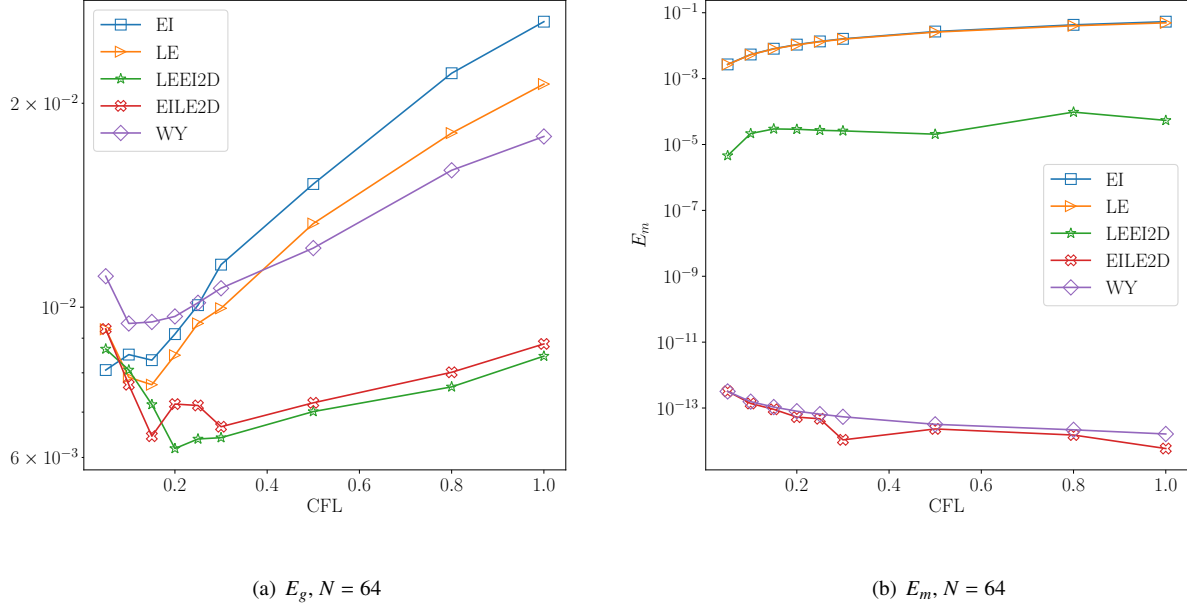
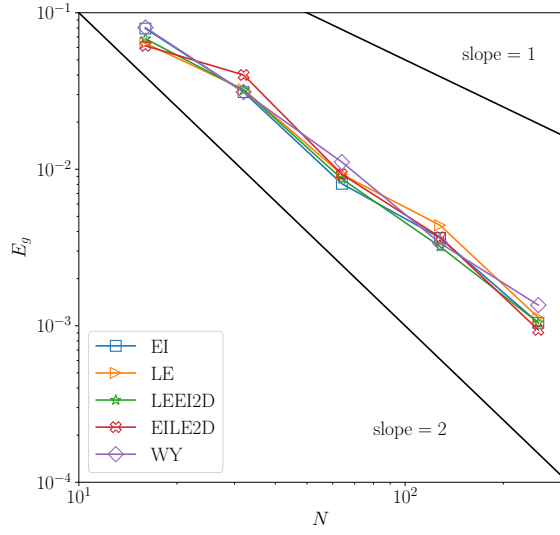


Figure 11: Geometric error and mass error of 2D Roder-Kothe single vortex test with repeatedly halving grid resolution with CFL numbers of 0.05 and 1.0. The corresponding data is shown in Table 6 and Table 7.

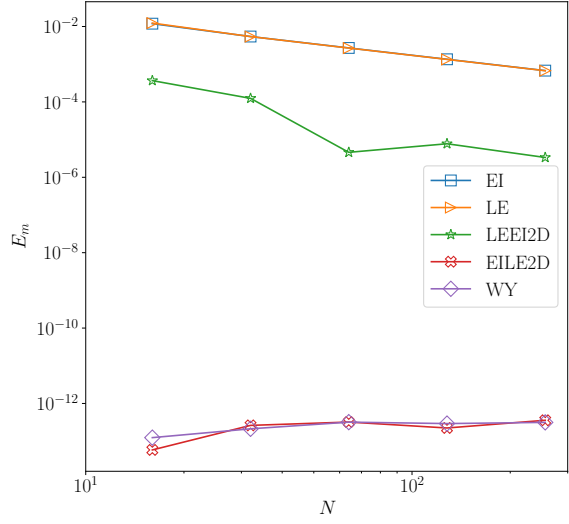
vortex is set to 4 in this study, which means a matrix of 4 vortex in the computational domain. The domain-centered circular suffers a even more severe deformation than that in Rider-Kothe single vortex test. As shown in Fig. 13, when $t = T/2$, although the material interface remains simply connected, some of the filament of the interface are very thin. When the period $T = 2$, the width of the thin filament can be as small as 2×10^{-4} . When the grid resolution is not enough, the material interface will tear. Similar to the Rider-Kothe single vortex test, this deformation test contains the computational cases with $CFL = 0.8$ and $CFL = 1.0$ as well.

When the grid resolution is 64×64 , the material interfaces with different CFL number at $t = T/2$ and $t = T$ are plotted in Fig. 10. When $t = T/2$, teared material material interfaces are observed for all methods. However, all methods remains good agreement with the main body of the material domain around center of the computational domain. At the time $t = T$, when CFL number is small (0.05), all methods recover to the initial shape with reasonable solution and do not show much difference between each other. When the CFL number is larger, EI and LE methods show a larger deviation with the exact solution, while the other three methods shows better agreement.

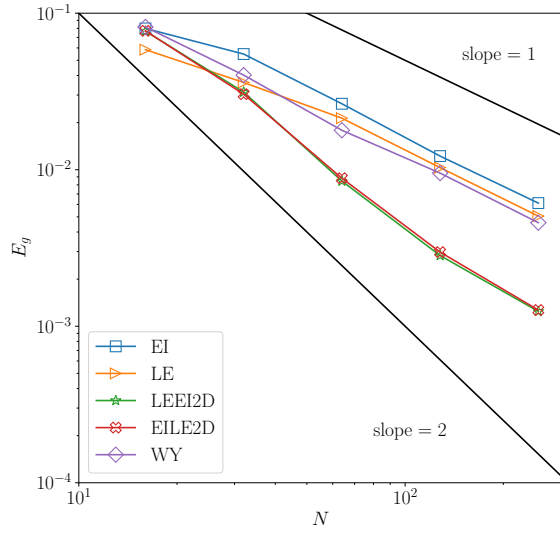
The geometrical error and mass conservation error with grid resolution of 64×64 are plotted in Fig. 15. The overall tendency of the the geometrical error with the change of CFL number is to decrease when the CFL number is getting smaller. The EI methods has the overall maximum error among all methods, LE and WY methods comes after with similar magnitude of of gemertric error. The EILE2D method has similar performance to LE and WY method when $CFL \leq 0.25$, and performs better when $CFL > 0.25$. The LEEI2D method has the overall minimum error among all



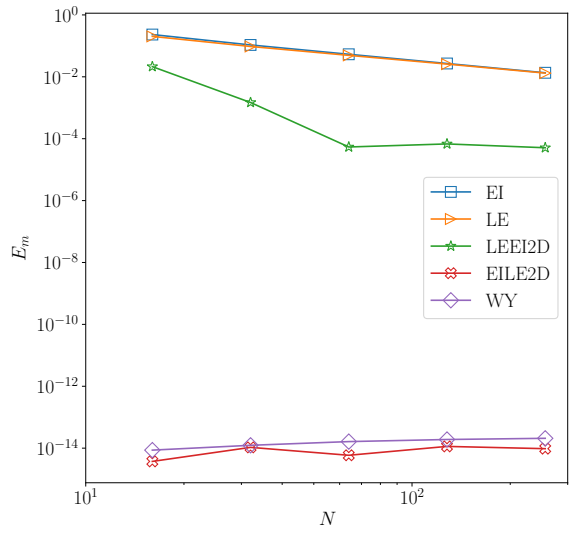
(a) E_g , CFL= 0.05



(b) E_m , CFL= 0.05



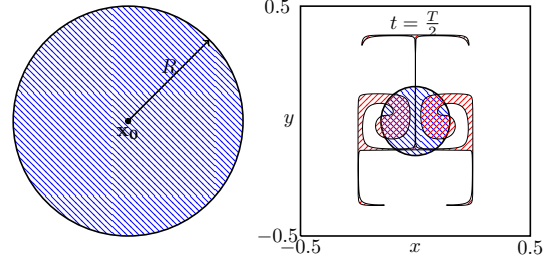
(c) E_g , CFL= 1.0



(d) E_m , CFL= 1.0

Figure 12: (a) Geometrical error and (b) mass error of 2D Roder-Kothe single vortex test with repeatedly halving grid resolution. The corresponding data is shown in Table 8 and Table 9.

Parameter	value
domain	$[-0.5, 0.5] \times [-0.5, 0.5]$
grids	$N \times N$
grid size	$h = 1/N$
shape	$\mathbf{x}_0 = (0, 0)$
Resolution	$R = 0.15$
CFL	$N \in \{16, 32, 64, 128, 256\}$
Time step	$c_f \in \{0.01, 0.05, 0.1, 0.15, 0.2, 0.25, 0.3, 0.5, 0.8, 1.0\}$
n_{step}	$k = c_f/N$
Velocity field	$6N/c_f$
Stream function	
Period	$\psi(x, y) = \frac{1}{n\pi} \sin(n\pi x) \cos(n\pi y) \cos\left(\frac{\pi t}{T}\right)$
	$T = 6$



(a) Initial and final geometry (b) Evolution of reverse vortex test

Figure 13: Initial setup and parameters of 2D reversed vortex test

methods. The EI method has the largest mass error, and LE method comes after. The LEEI2D method improves the mass conservation of the EI and LE methods. The EILE2D method preserves mass to machine precision for all CFL numbers in the test cases. The WY methods loses its ultimate mass preserving at CFL = 0.8 and CFL = 1.0. Even for the case when WY methods loses its ultimate mass conservation, the mass error is smaller than EI, LE and LEEI2D methods.

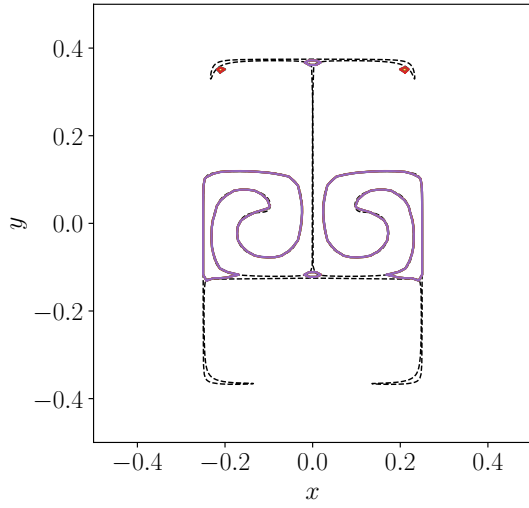
The change of geometrical error and mass error with the grid resolution are plotted in Fig. 16. Again, when CFL number is small (CFL=0.05 as shown in Figs. 16 (a) and (b)), the geometrical error are similar to each other for all methods, both WY and EILE2D method conserve mass to machine precision. LEEI2D method show a better mass conservation than EI and LE methods. When CFL number is large (CFL=1.0 as shown in Figs. 16 (c) and (d)), LEEI2D method has the best performance on geometrical error, and better mass conservation than EI and LE method. The EILE2D method ultimately conserve mass and has the second best performance on geometrical error. The WY method, which is similar performance on geometric error, no longer preserve mass when CFL = 1. However, the WY has a better performance on mass conservation than the LEEI2D method.

6.2. 3D tests

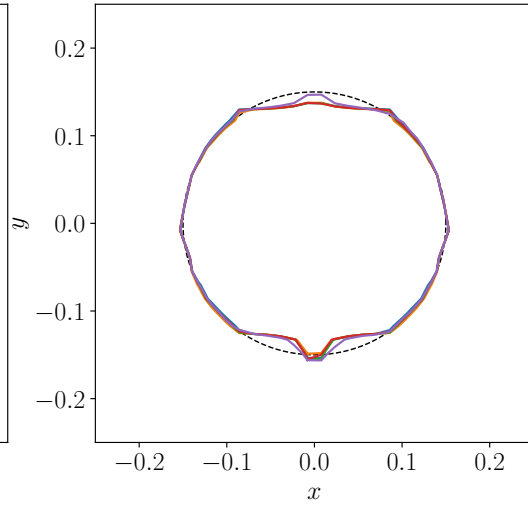
6.2.1. Zalesak's disk rotation test

Similar to the 2D Zalesak's in subsection 6.1.1, the 3D Zalesak's rotation test extends the slotted disk to a 3D slotted sphere [36]. The x and y component of the velocity remains the 2D rotation field and a uniform velocity is applied to the z component of the velocity field. The initial setup and the velocity field are shown in Fig. 17. Periodic boundary condition is applied at z direction.

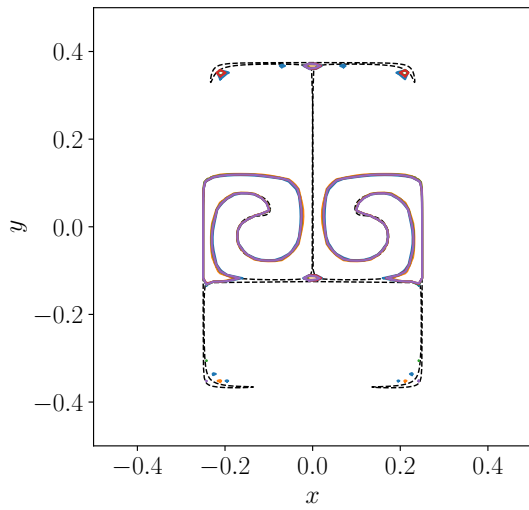
The results from different methods are plotted in Fig. 18. Similar to the 2D result, the geometrical error decreases when the CFL number becomes larger. When the grid resolution increases, again, the geometrical error decreases. Most of the methods do not show significant difference between each other, except for the EILE3D method. This could be explained that the velocity magnitude of three divergence-free 2D is about a half of the original velocity



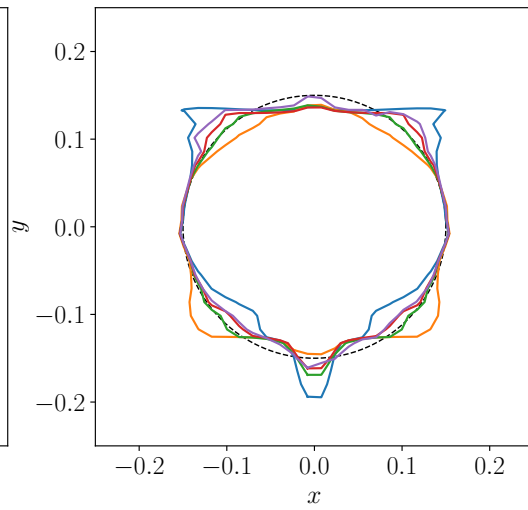
(a) $t = T/2$, CFL = 0.05



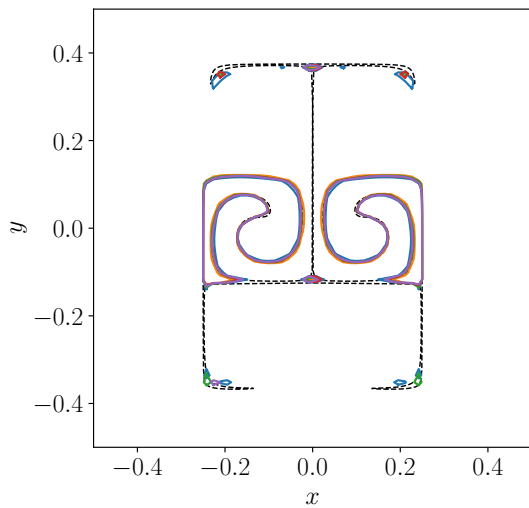
(b) $t = T$, CFL = 0.05



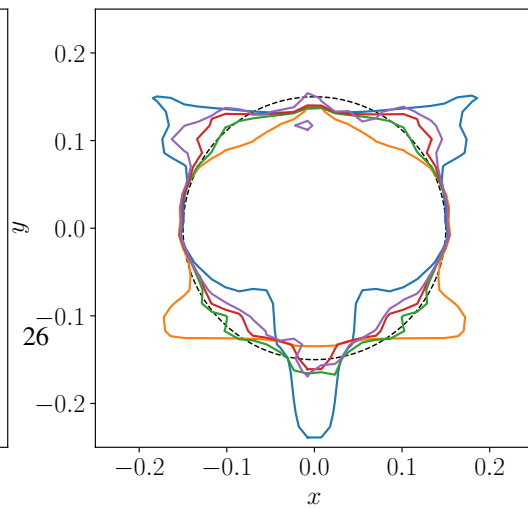
(c) $t = T/2$, CFL = 0.5



(d) $t = T$, CFL = 0.5



(e) $t = T/2$, CFL = 1.0



(f) $t = T$, CFL = 1.0

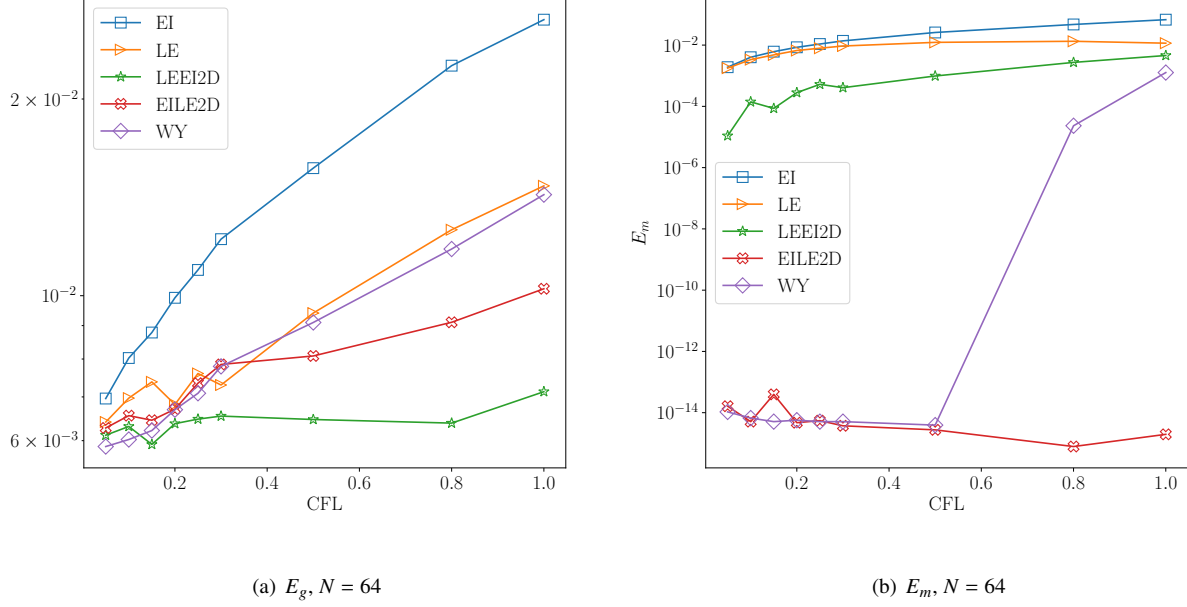


Figure 15: (a) Geometric error and (b) mass error of 2D reversed vortex test with repeatedly halving grid resolution. The corresponding data is shown in Table 10 and Table 11.

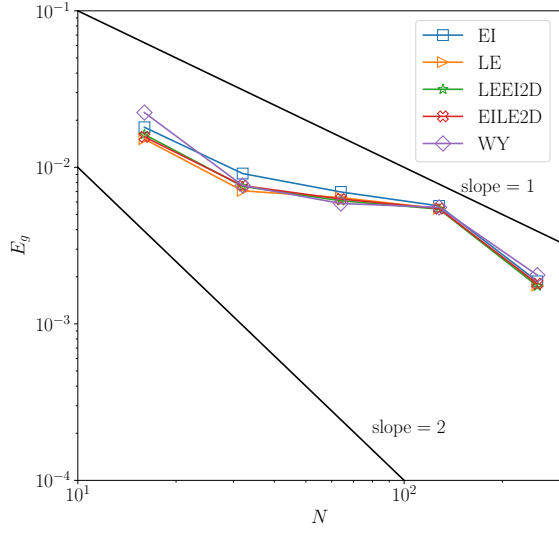
field. While the velocity magnitude is halved, the equivalent CFL numbers are halved as well, leading to a larger geometrical error as the relationship between the geometrical error and CFL number shown in Fig. 19. For the mass error, all results converge to machine precision, which remains the same as the 2D problem.

6.2.2. Single vortex test

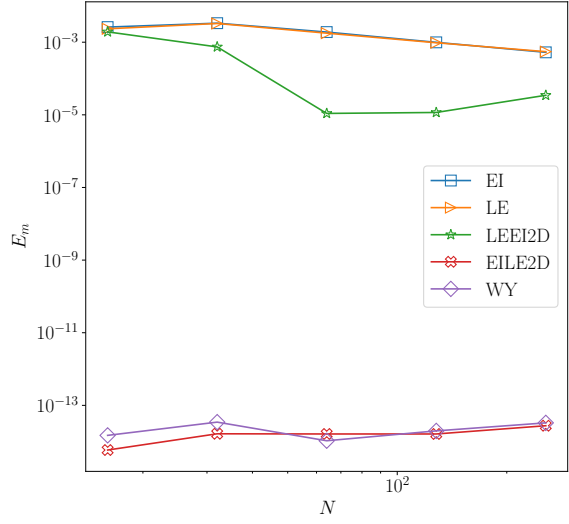
The 2D Rider-Kothe single vortex problem is extended to 3D with several approaches [37, 24, 26]. The divergence-free velocity field of 3D single vortex test by Liovic et al. [37] is used in this study. The initial set up and test parameters are shown in Fig. 20. The x, y component of the velocity field is identical to the 2D Rider-Kothe single vortex test, and the additional velocity component is a laminar pipe flow.

The material interface at $t = T/2$ and $t = T$ with grid resolution $N = 64$ is shown in Fig. 21 and Fig. 22. The exact results in Fig. 21 (a) and Fig. 22 (a) are calculated with analytical marker particles. At $t = T/2$, all results do not have significant visual difference. At $t = T$, all results look similar with each other, except for the EI result.

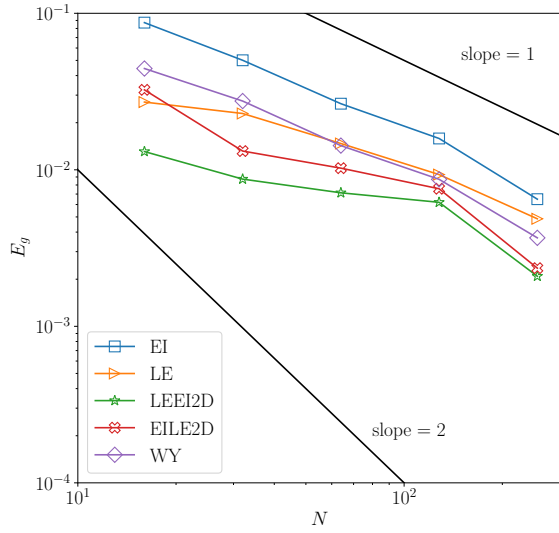
Fig. 23 shows the effect on the solution accuracy and mass conservation with CFL number when the grid resolution is $32 \times 32 \times 64$. Using the velocity decomposition of Eq. (41) on the velocity field in Fig. 20, the maximum magnitude of the velocity field could be as big as about 3.0, which means the equivalent maximum CFL is tripled after velocity decomposition. In Fig. 23 (a), when $CFL \geq 0.5$, unreasonable results lead to a spike on mass and geometrical error. Among the rest of 5 methods, EI method has the most significant geometrical error, while the geometrical error



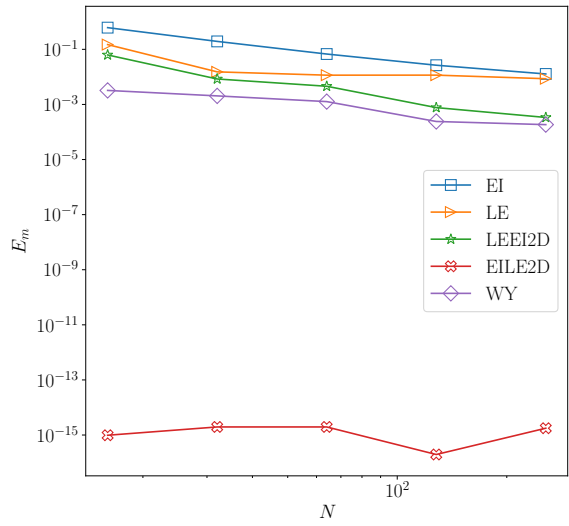
(a) E_g , CFL= 0.05



(b) E_m , CFL= 0.05



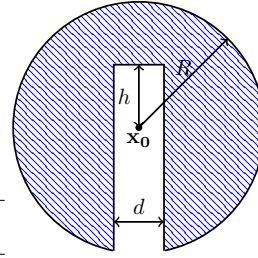
(c) E_g , CFL= 1.0



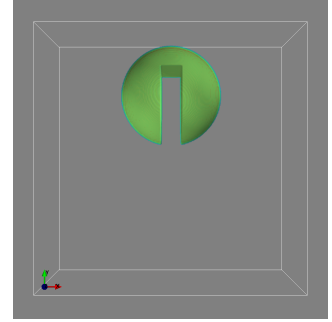
(d) E_m , CFL= 1.0

Figure 16: Geometric error and mass error of 2D reversed vortex test with different CFL numbers on a 64×64 mesh. The corresponding data in shown in Table 12 and Table 13.

Parameter	value
domain	$[0, 1] \times [0, 1] \times [0, 0.5]$
grids	$N \times N \times N/2$
grid size	$h = 1/N$
shape	$\mathbf{x}_0 = (0.5, 0.75, 0.25)$ $R = 0.2, h = 0.1$ $d = 0.08$
Resolution	$N \in [16, 32, 64, 128, 256]$
CFL	$c_f \in [0.01, 0.05, 0.1, 0.15, 0.2, 0.25, 0.3, 0.5]$
Time step	$k = 2c_f/N$
n_{step}	$3N/c_f$
Velocity field	
Velocity	$u(x, y, z) = \frac{2\omega}{T}(x - x_0)$ $v(x, y, z) = \frac{2\omega}{T}(y - y_0)$ $w = 0.5$
Period	$T = 6$
Angular velocity	$\omega = 0.5$



(a) 2D slice at $z = 0.25$



(b) 3D view

Figure 17: Initial setup and parameters of 3D Zalesak's rotation test.

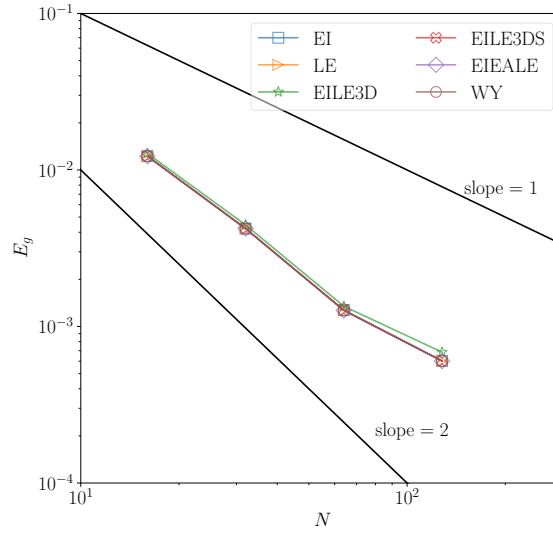


Figure 18: Geometric error with the repeatedly halving grid resolution under a CFL number of 0.03. The corresponding data is shown in Table 14.

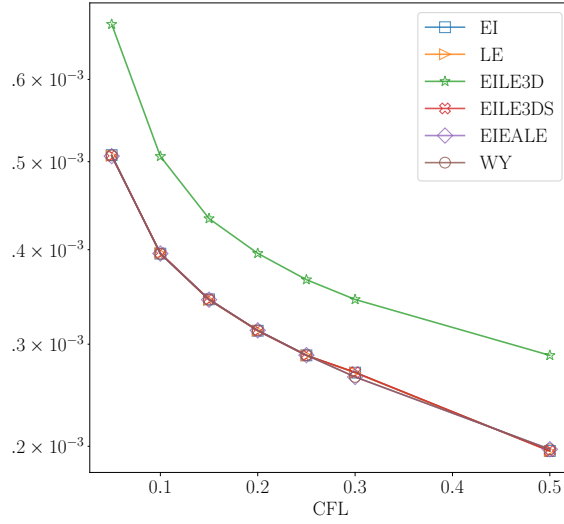
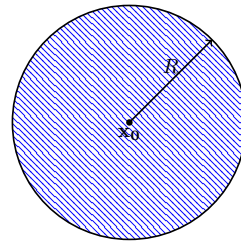
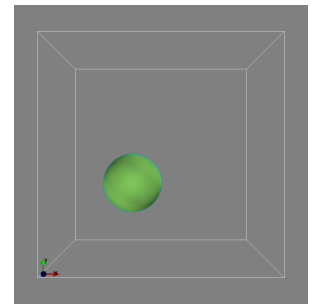


Figure 19: Geometric error with the change of CFL number on a $64 \times 64 \times 64$ mesh. The corresponding data is shown in Table 15.

Parameter	value
domain	$[0, 1] \times [0, 1] \times [0, 1]$
grids	$N \times N \times N$
grid size	$h = 1/N$
shape	$\mathbf{x}_0 = (0.5, 0.25, 0.5)$
Time step	$k = 1/N$
n_{step}	$6N$
Resolution	$N \in \{16, 32, 64, 128, 256\}$
CFL	$c_f \in \{0.01, 0.05, 0.1, 0.15, 0.2, 0.25, 0.3, 0.5, 0.8, 1.0\}$
Velocity Field	
Velocity	$u(x, y, z) = \sin(2\pi y) \sin^2(\pi x) \cos\left(\frac{\pi t}{T}\right)$ $v(x, y, z) = -\sin(2\pi x) \sin^2(\pi y) \cos\left(\frac{\pi t}{T}\right)$ $w(x, y, z) = \left(1 - \frac{r}{R}\right)^2 \cos\left(\frac{\pi t}{T}\right)$
Period	$T = 3$
R	$R = 0.5$
r	$r = \sqrt{(x-0.5)^2 + (y-0.5)^2}$



(a) 2D view



(b) 3D view

Figure 20: Initial setup and parameters of 3D single vortex test.

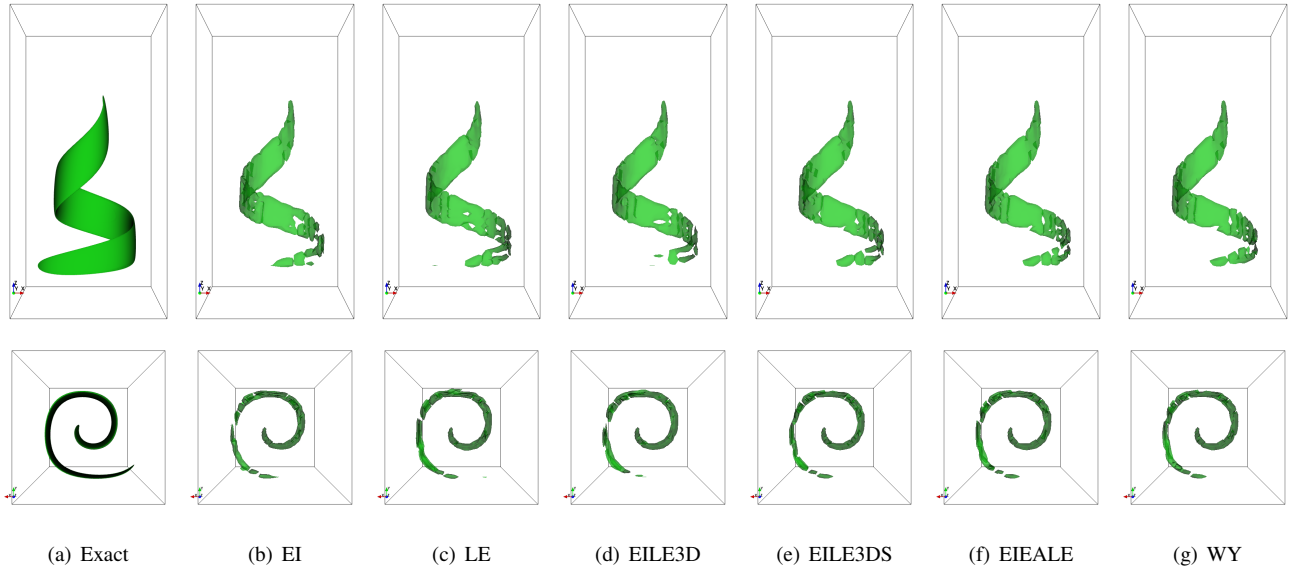


Figure 21: Front view (First row) and vertical view (Second row) of the material interface of 3D Rider-Kothe single vortex test at $t = T/2$ with grid resolution of $32 \times 32 \times 64$.

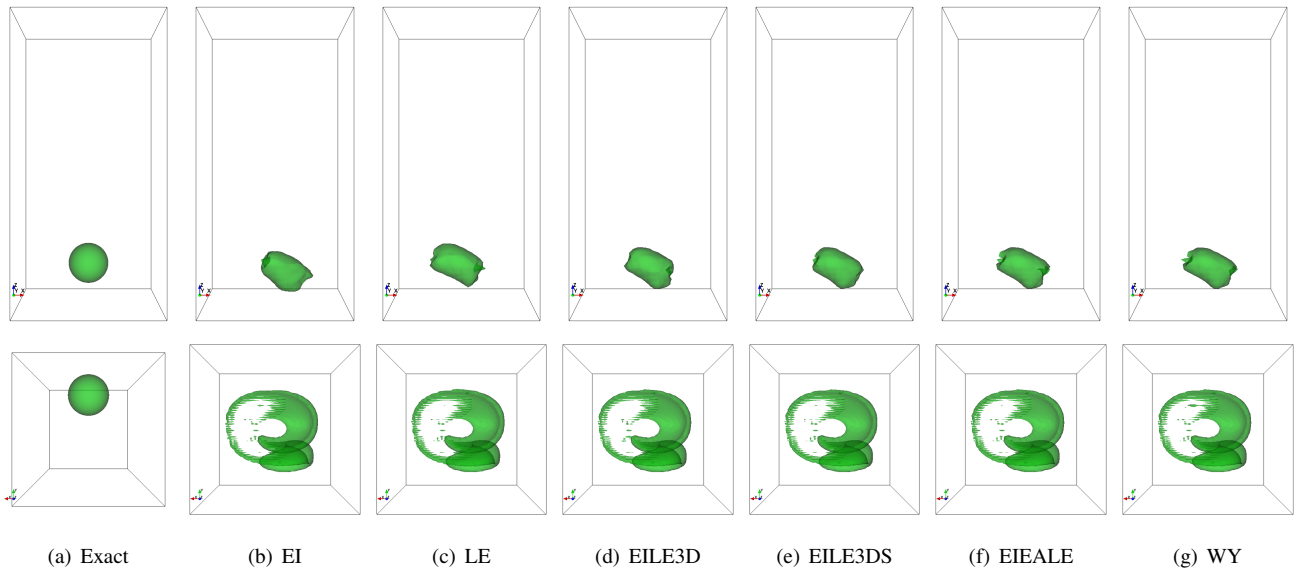


Figure 22: Front view (First row) and vertical view (Second row) of the material interface of 3D Rider-Kothe single vortex test at $t = T$ with grid resolution of $32 \times 32 \times 64$.

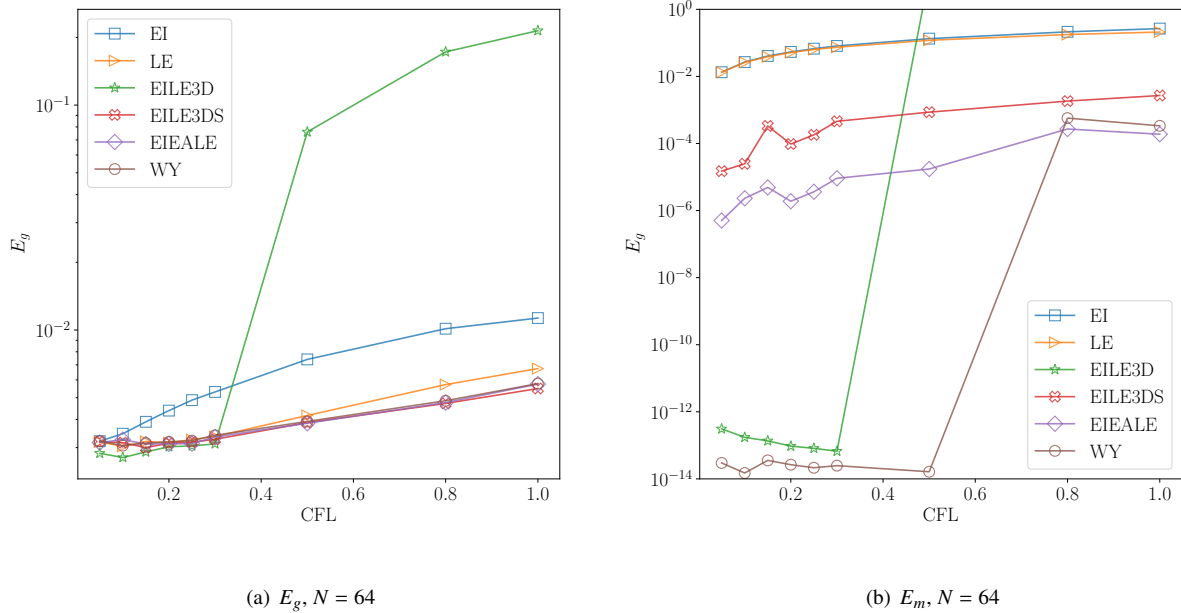


Figure 23: (a) Geometric error and (b) mass error of 3D reversed vortex test with the change of CFL number on a $32 \times 32 \times 64$ mesh. The corresponding data in shown in Table 16 and Table 17.

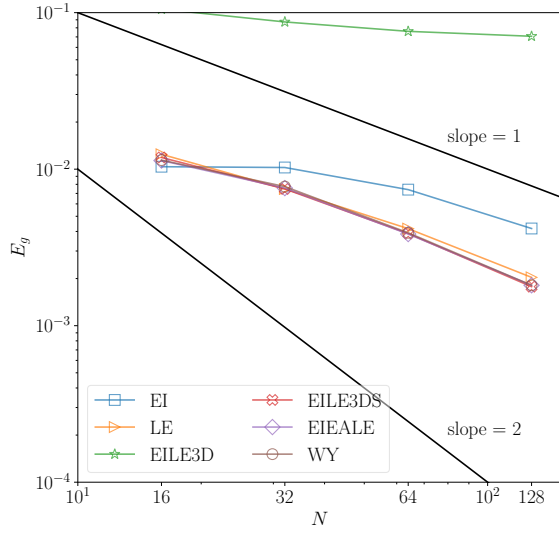
of LE methods is smaller than EI methods. EILE3DS, EIEALE and WY methods has very similar performance on geometrical error and better than those of EI and LE method. For mass conservation, EIEALE conserves mass with higher order of mass loss than EILE3DS method. WY method conserves mass to machine precision CFL < 0.5, for a larger CFL number, the WY methods no longer conserves mass to machine precision. However, the mass error is very close to the EIEALE method and better than the rest of the methods.

The effect on the solution accuracy and mass conservation with repeat halving the grid resolution is shown in Fig. 24. Note that most of the EILE3D results are out of the plot range. With different grid resolution under two CFL numbers (0.3 and 1.0). Considering that the velocity decomposition leads to the stability issues on EILE3DS methods, WY method shows an overall best performance on mass conservation.

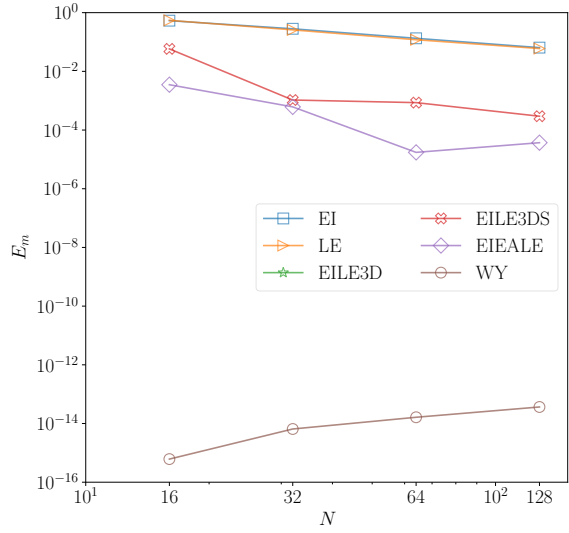
6.2.3. Reverse Vortex test

A more stringent 3D test: reversed vortex test [35] is taken in this subsection. The initial set up and test parameters are shown in Fig. 25. Under the two rotating vortices, the initial material of sphere scoops out and pancake, leading to a very thin and stretched interface at $t = T/2$ (See Fig. 26(a)), and recovers to the initial sphere at $t = T$ (See Fig. 27(a)). When the grid resolution is not fine enough, part of the interface may thin out of the grid resolution, leading to a massive of fragmentation and coalescence. When recovered the initial position at $t = T$ (See Fig. 26 and Fig. 27).

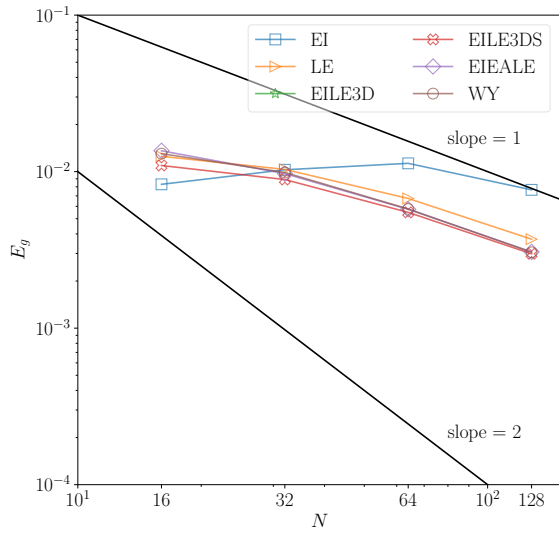
Fig. 28 shows the effect on the solution accuracy and mass conservation with CFL number when the grid resolution



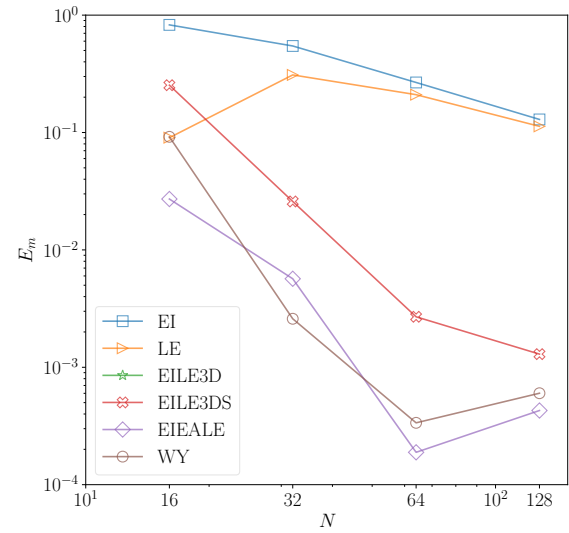
(a) E_g , CFL= 0.05



(b) E_m , CFL= 0.05



(c) E_g , CFL= 1.0



(d) E_m , CFL= 1.0

Figure 24: Geometric error and mass error of 3D reversed vortex test with repeated halving grid resolution under CFL number of 0.3 and 1.0. The corresponding data in shown in Table 18 and Table 19.

Parameter	value
domain	$[0, 1] \times [0, 1] \times [0, 1]$
Resolution	$N = 50, 100, 200$
grids	$N \times N \times N$
grid size	$h = 1/N$
Period	$T = 3.0$
shape	$\mathbf{x}_0 = (0.35, 0.35, 0.35)$
	$R = 0.15$
$u(x, y, z)$	$2 \sin^2(\pi x) \sin(2\pi y) \sin(2\pi z) \cos(\pi t/T)$
$v(x, y, z)$	$-\sin(2\pi x) \sin^2(\pi y) \sin(2\pi z) \cos(\pi t/T)$
$w(x, y, z)$	$-\sin(2\pi x) \sin(2\pi y) \sin^2(\pi z) \cos(\pi t/T)$
Time step	$k = 1/N$
n_{step}	$6N$
CFL number	0.2

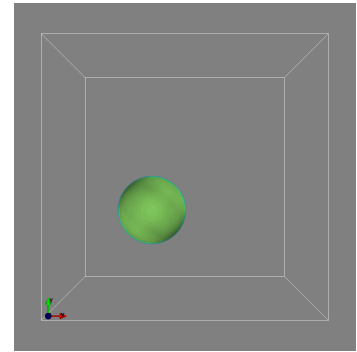
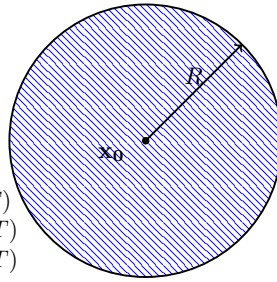


Figure 25: Initial setup and parameters of 3D reversed vortex rotation test

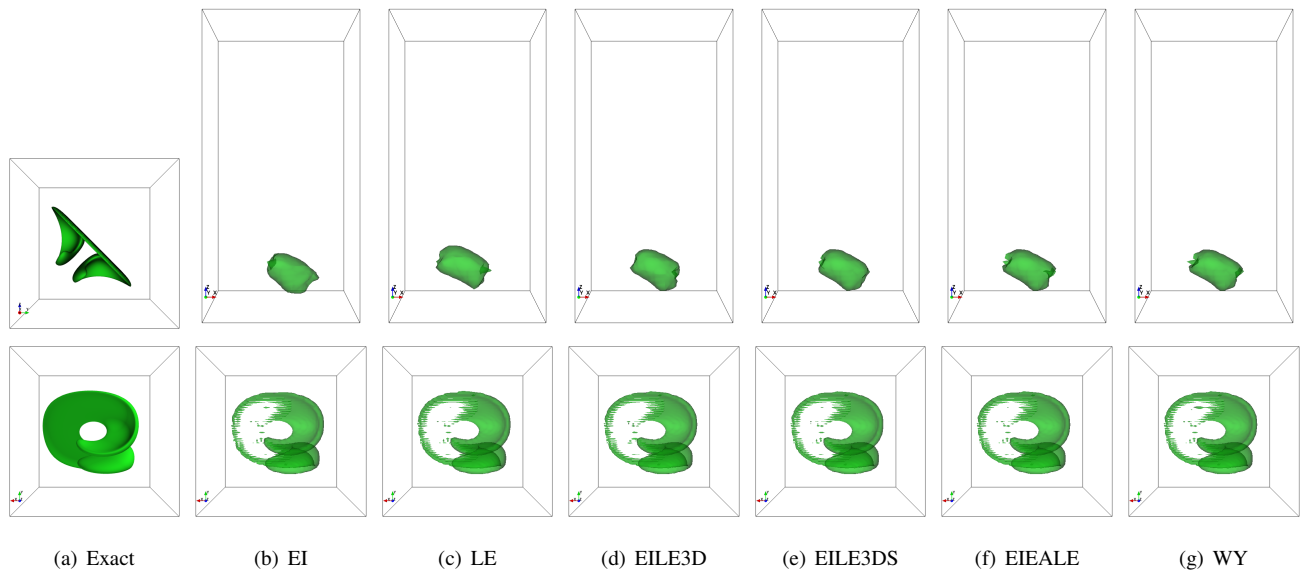


Figure 26: Front view (First row) and vertical view (Second row) of the material interface of 3D reversed vortex test at $t = T/2$ with grid resolution of $64 \times 64 \times 64$.

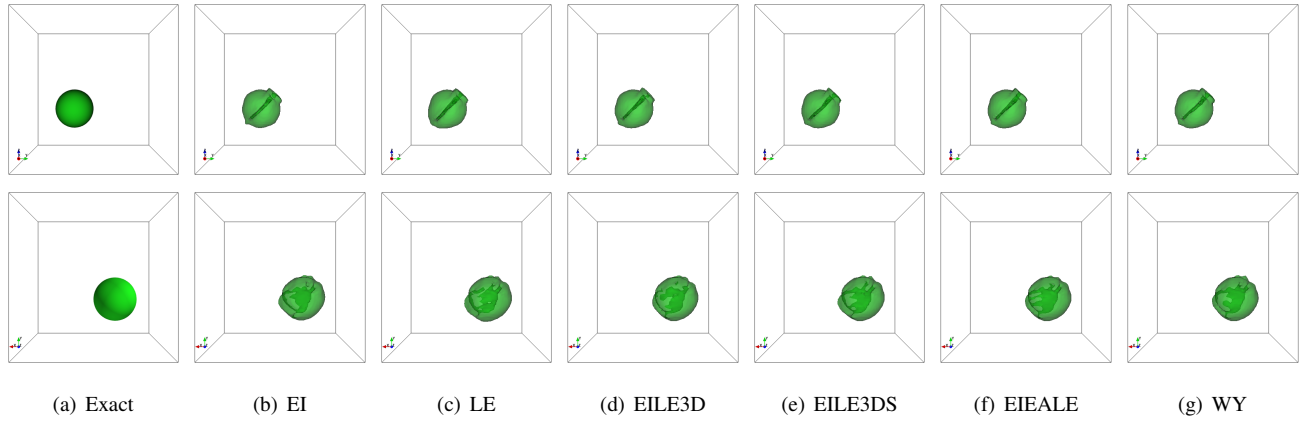
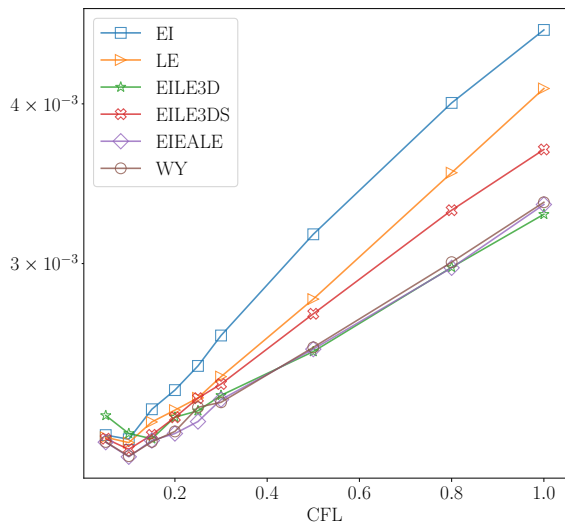
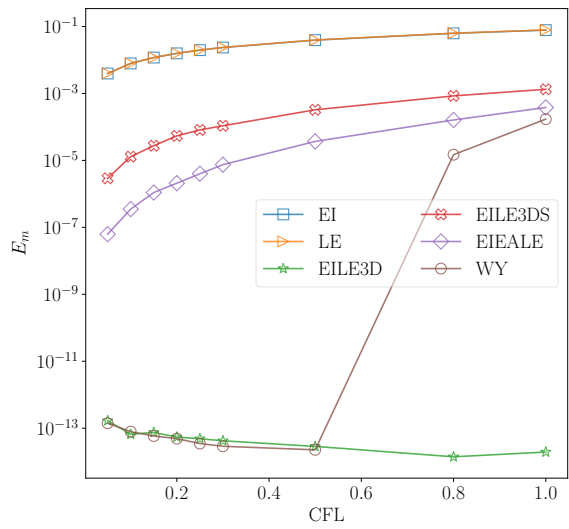


Figure 27: Front view (First row) and vertical view (Second row) of the material interface of 3D reversed vortex test at $t = T$ with grid resolution of $64 \times 64 \times 64$.



(a) $E_g, N = 64$



(b) $E_m, N = 64$

Figure 28: (a) Geometric error and (b) mass error of 3D reversed vortex test with the change of CFL number on a $64 \times 64 \times 64$ mesh. The corresponding data is shown in Table 20 and Table 21.

is $64 \times 64 \times 64$. Unlike the velocity field in Section 6.2.2, when applying the velocity decomposition of Eq. (41) applied on the Fig. 20, the maximum magnitude of the velocity is about 0.5, which is about a half of the original velocity field. The velocity decomposition of Eq. (41) will not bring in the stability issue for the velocity field shown in Fig. 25. The EILE3D methods always conserve mass to machine precision and performs as one of the best methods among all six candidate methods on geometrical error. The EIEALE and WY methods has similar performance on geometrical error. When $CFL \leq 0.5$, WY method conserves mass to machine precision, and has a slightly smaller mass error compared with the EILE method. The EI and LE methods again has the worst mass conservation, and LE method has smaller geometrical error than the EI methods. the EILE3D method, although improves the mass the geometrical error over EI and LE methods, is not as good as EIEALE, WY or EILE3D method in this test.

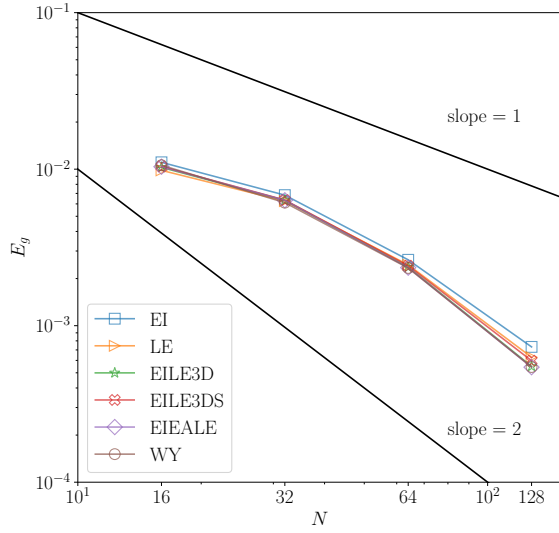
The effect on the solution accuracy and mass conservation with repeat halving the grid resolution is shown in Fig. 29. The EILE3D method has the overall best performance on mass conservation and geometrical error. The WY method has similar performance with the EILE3D method, except for the mass conservation on large CFL number. However, even when unconserved mass occur due to the large CFL number, WY method is one of the best method on mass conservation among the rest of the methods exclude EILE3D method. WY method improves the mass conservation by the order of $O(10^{-2}) - O(10^{-4})$ compared with EI and LE methods.

7. Conclusion

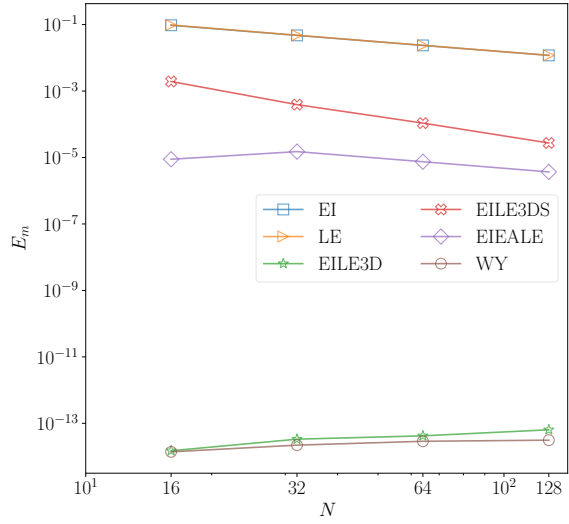
In this study, a comparative study on several flux-splitting MOF methods are carried out. Several directional splitting methods has been extended from VOF-PLIC to MOF advection. These methods, along with several existing split MOF advection methods, are investigated in both 2D and 3D. We focus on the three important conditions for MOF advection: (1) global mass conservation condition, (2) local bounded condition (3) geometrical consistency condition. Six numerical tests cases are used to evaluate the geometrical and mass conservation for different MOF advection methods. Besides, we also derived a fast and efficient formulation for calculating the volume and centroid from known equation of plane.

For 2D problem, the hybrid Eulerian Implicit and Lagrangian Explicit (EI-LE) strategy is the only strategy that satisfies all three conditions. The EI-LE strategy in 2D (EILE2D) is ultimately mass conservation and geometrical conservation. The EILE2D method has also obtained the overall best performance on geometrical error. For 2D problem, EILE2D method is recommended for MOF advection.

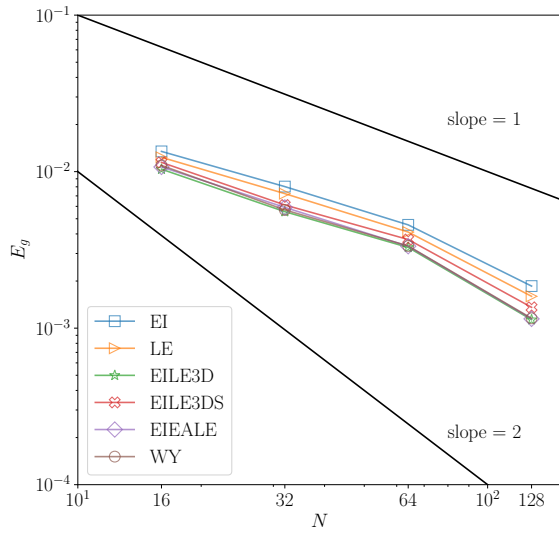
The implementation of EI-LE strategy in 3D (EILE3D) is not as straightforward as its in 2D. The EILE3D method need to decomposed the original velocity field into 3 2D divergence-free velocity fields, which is equivalent with 3 EILE2D advection. Thus three conditions holds for EILE3D. However, the numerical tests show that the velocity decomposition may bring in stability issue. The Weymouth-Yue strategy (WY) is ultimately mass conservation, although it does not guarantee the geometrical consistency, the overall performance on geometrical error is one of the best among all split advection methods in this study. While the WY method has a more stringent CFL limit of $1/6$



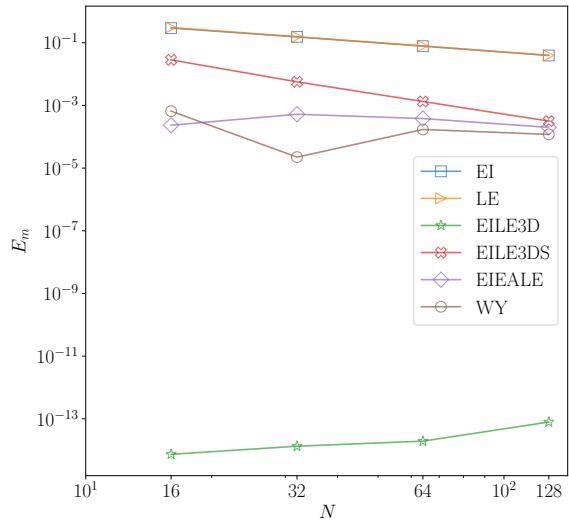
(a) E_g , CFL= 0.3



(b) E_m , CFL= 0.3



(c) E_g , CFL= 1.0



(d) E_m , CFL= 1.0

Figure 29: Geometric error and mass error of 3D reversed vortex test with repeated halving grid resolution under CFL number of 0.3 and 1.0. The corresponding data is shown in Table 22 and Table 23.

in order to guarantee an ultimate mass conservation. Numerical tests show that for a larger CFL number, although WY method no longer preserve mass to machine precision, it still significantly improves the mass conservation from EI or LE methods. Considering the overall performance on mass conservation and geometrical error, along with the stability issue, WY methods is preferable for 3D problems.

References

- [1] E. Aulisa, S. Manservigi, R. Scardovelli, S. Zaleski, A geometrical area-preserving Volume-of-Fluid advection method, *Journal of Computational Physics* 192 (2003) 355–364.
- [2] W. F. Noh, P. Woodward, SLIC (Simple Line Interface Calculation), in: J. Ehlers, K. Hepp, H. A. Weidenmüller, J. Zittartz, W. Beiglböck, A. I. van de Vooren, P. J. Zandbergen (Eds.), *Proceedings of the Fifth International Conference on Numerical Methods in Fluid Dynamics June 28 – July 2, 1976 Twente University, Enschede*, volume 59, Springer Berlin Heidelberg, Berlin, Heidelberg, 1976, pp. 330–340. URL: http://link.springer.com/10.1007/3-540-08004-X_336. doi:10.1007/3-540-08004-X_336.
- [3] C. Hirt, B. Nichols, Volume of fluid (VOF) method for the dynamics of free boundaries, *Journal of Computational Physics* 39 (1981) 201–225. Number: 1.
- [4] D. L. Youngs, *Time-dependent multi-material flow with large fluid distortion*, Numerical methods for fluid dynamics (1982). Publisher: Academic Press.
- [5] Q. Zhang, P. L.-F. Liu, A new interface tracking method: The polygonal area mapping method, *Journal of Computational Physics* 227 (2008) 4063–4088.
- [6] T. Marić, D. B. Kothe, D. Bothe, Unstructured un-split geometrical Volume-of-Fluid methods – A review, *Journal of Computational Physics* 420 (2020) 109695.
- [7] V. Dyadechko, M. Shashkov, Moment-of-fluid interface reconstruction, Los Alamos Report LA-UR-05-7571 (2005).
- [8] H. T. Ahn, M. Shashkov, Multi-material interface reconstruction on generalized polyhedral meshes, *Journal of Computational Physics* 226 (2007) 2096–2132. Number: 2.
- [9] M. Jemison, E. Loch, M. Sussman, M. Shashkov, M. Arienti, M. Ohta, Y. Wang, A Coupled Level Set-Moment of Fluid Method for Incompressible Two-Phase Flows, *Journal of Scientific Computing* 54 (2013) 454–491. Number: 2-3.
- [10] Y. Liu, M. Sussman, Y. Lian, M. Yousuff Hussaini, A moment-of-fluid method for diffusion equations on irregular domains in multi-material systems, *Journal of Computational Physics* 402 (2020) 109017.
- [11] S. Galera, J. Breil, P.-H. Maire, A 2D unstructured multi-material Cell-Centered Arbitrary Lagrangian–Eulerian (CCALE) scheme using MOF interface reconstruction, *Computers & Fluids* 46 (2011) 237–244.
- [12] J. Breil, T. Harribey, P.-H. Maire, M. Shashkov, A multi-material ReALE method with MOF interface reconstruction, *Computers & Fluids* 83 (2013) 115–125.
- [13] X. Chen, X. Zhang, An improved 3D MoF method based on analytical partial derivatives, *Journal of Computational Physics* 326 (2016) 156–170.
- [14] A. Lemoine, S. Glockner, J. Breil, Moment-of-fluid analytic reconstruction on 2D Cartesian grids, *Journal of Computational Physics* 328 (2017) 131–139.
- [15] T. Milcent, A. Lemoine, Moment-of-fluid analytic reconstruction on 3D rectangular hexahedrons, *Journal of Computational Physics* 409 (2020) 109346.
- [16] S. Bnà, A. Cervone, V. Le Chenadec, S. Manservigi, R. Scardovelli, Review of split and unsplit geometric advection algorithms, Rhodes, Greece, 2013, pp. 875–878. URL: <http://aip.scitation.org/doi/abs/10.1063/1.4825636>. doi:10.1063/1.4825636.
- [17] M. Jemison, M. Sussman, M. Arienti, Compressible, multiphase semi-implicit method with moment of fluid interface representation, *Journal of Computational Physics* 279 (2014) 182–217.

- [18] A. Asuri Mukundan, T. Ménard, J. C. Brändle de Motta, A. Berlemont, A 3D Moment of Fluid method for simulating complex turbulent multiphase flows, *Computers & Fluids* 198 (2020) 104364.
- [19] V. Dyadechko, M. Shashkov, Reconstruction of multi-material interfaces from moment data, *Journal of Computational Physics* 227 (2008) 5361–5384.
- [20] R. Scardovelli, S. Zaleski, Interface reconstruction with least-square fit and split Eulerian-Lagrangian advection, *International Journal for Numerical Methods in Fluids* 41 (2003) 251–274.
- [21] R. Scardovelli, S. Zaleski, Analytical Relations Connecting Linear Interfaces and Volume Fractions in Rectangular Grids, *Journal of Computational Physics* 164 (2000) 228–237. Number: 1.
- [22] W. J. Rider, D. B. Kothe, Reconstructing Volume Tracking, *Journal of Computational Physics* 141 (1998) 112–152.
- [23] G. Li, Y. Lian, Y. Guo, M. Jemison, M. Sussman, T. Helms, M. Arienti, Incompressible multiphase flow and encapsulation simulations using the moment-of-fluid method: Incompressible multiphase flow and encapsulation simulations using the moment-of-fluid method, *International Journal for Numerical Methods in Fluids* 79 (2015) 456–490.
- [24] E. Aulisa, S. Manservigi, R. Scardovelli, S. Zaleski, Interface reconstruction with least-squares fit and split advection in three-dimensional Cartesian geometry, *Journal of Computational Physics* 225 (2007) 2301–2319. Number: 2.
- [25] G. Weymouth, D. K.-P. Yue, Conservative Volume-of-Fluid method for free-surface simulations on Cartesian-grids, *Journal of Computational Physics* 229 (2010) 2853–2865.
- [26] A. Baraldi, M. Dodd, A. Ferrante, A mass-conserving volume-of-fluid method: Volume tracking and droplet surface-tension in incompressible isotropic turbulence, *Computers & Fluids* 96 (2014) 322–337.
- [27] A. Nijenhuis, H. S. Wilf, *Combinatorial algorithms: for computers and calculators*, Elsevier, 2014.
- [28] H. T. Ahn, M. Shashkov, Geometric algorithms for 3D interface reconstruction, in: *Proceedings of the 16th international meshing roundtable*, Springer, 2008, pp. 405–422.
- [29] J. López, J. Hernández, Analytical and geometrical tools for 3D volume of fluid methods in general grids, *Journal of Computational Physics* 227 (2008) 5939–5948.
- [30] S. Diot, M. François, E. Dendy, An interface reconstruction method based on analytical formulae for 2D planar and axisymmetric arbitrary convex cells, *Journal of Computational Physics* 275 (2014) 53–64.
- [31] S. Diot, M. M. François, An interface reconstruction method based on an analytical formula for 3D arbitrary convex cells, *Journal of Computational Physics* 305 (2016) 63–74.
- [32] X. Yang, A. J. James, Analytic relations for reconstructing piecewise linear interfaces in triangular and tetrahedral grids, *Journal of Computational Physics* 214 (2006) 41–54.
- [33] S. T. Zalesak, Fully multidimensional flux-corrected transport algorithms for fluids, *Journal of computational physics* 31 (1979) 335–362.
- [34] M. Rudman, VOLUME-TRACKING METHODS FOR INTERFACIAL FLOW CALCULATIONS, *International Journal for Numerical Methods in Fluids* 24 (1997) 671–691.
- [35] R. J. LeVeque, High-Resolution Conservative Algorithms for Advection in Incompressible Flow, *SIAM Journal on Numerical Analysis* 33 (1996) 627–665.
- [36] D. Enright, R. Fedkiw, J. Ferziger, I. Mitchell, A Hybrid Particle Level Set Method for Improved Interface Capturing, *Journal of Computational Physics* 183 (2002) 83–116. Number: 1.
- [37] P. Liovic, M. Rudman, J.-L. Liow, D. Lakehal, D. Kothe, A 3D unsplit-advection volume tracking algorithm with planarity-preserving interface reconstruction, *Computers & Fluids* 35 (2006) 1011–1032.

Appendix A: Triangular cutting plane

Configuration 1: Triangle cut interface

This configuration is the simplest one as all intercepts of the x_i coordinates are within the range of the hexahedron. The cutting interface is a triangle. The volume and corresponding centroid are expressed as

$$V = \frac{\alpha^3}{6m_1m_2m_3} \quad (55)$$

and the corresponding centroid is expressed as

$$\begin{aligned} c_1 &= \frac{\alpha}{4m_1}, \\ c_2 &= \frac{\alpha}{4m_2}, \\ c_3 &= \frac{\alpha}{4m_3}. \end{aligned} \quad (56)$$

Configuration 2: Quadrilateral cutting interface

When $m_1 < \alpha < m_3$, the intercept on x_1 coordinate exceeds the range of of the hexahedron. The cutting interface is a quadrilateral. The cutting polyhedron can be determined by subtracting a smaller tetrahedron from the tetrahedron formed by the original point and three intercepts points. The volume and corresponding centroid are expressed as

$$V = \frac{A}{6m_1m_2m_3}, \quad (57)$$

$$\begin{aligned} c_1 &= \frac{3}{4} - \frac{\alpha(3\alpha - m_1)}{4A}, \\ c_2 &= \frac{(2\alpha - m_1)(\alpha^2 + (\alpha - m_1)^2)}{4A}, \\ c_3 &= \frac{(2\alpha - m_1)(\alpha^2 + (\alpha - m_1)^2)}{4A}, \end{aligned} \quad (58)$$

where

$$A = \alpha^3 - (\alpha - m_1)^3 - (\alpha - m_2)^3, \quad (59)$$

Configuration 3: Pentagon cutting interface

When $m_2 < \alpha < m_c$, where $m_c = \min(m_{12}, m_3)$ and $m_{12} = m_1 + m_2$, the intercept on x_1 and x_2 coordinates exceeds the range of of the hexahedron. The cutting interface is a pentagon. The cutting polyhedron can be determined by subtracting two smaller tetrahedron from the tetrahedron formed by the original point and three intercepts points. The volume and corresponding centroid are expressed as

$$V = \frac{A}{6m_1m_2m_3}, \quad (60)$$

$$\begin{aligned} c_1 &= -\frac{\alpha^4 - (\alpha - m_1)^3(\alpha + 3m_1) - (\alpha - m_2)^4}{4m_1A}, \\ c_2 &= -\frac{\alpha^4 - (\alpha - m_1)^4 - (\alpha - m_2)^3(\alpha + 3m_2)}{4m_2A}, \\ c_3 &= -\frac{\alpha^4 - (\alpha - m_1)^4 - (\alpha - m_2)^4}{4m_3A}, \end{aligned} \quad (61)$$

where

$$A = \alpha^3 - (\alpha - m_1)^3 - (\alpha - m_2)^3. \quad (62)$$

Configuration 4: Hexagon cutting interface

When $m_3 < m_{12}$ and $m_3 < \alpha < 1/2$, all intercepts on x_i coordinates exceeds the range of of the hexahedron. The cutting interface is a hexagon. The cutting polyhedron can be determined by subtracting three as smaller tetrahedron from the tetrahedron formed by the original ponit and three intercepts points. The volume and corresponding centroid are expressed as

$$V = \frac{A}{6m_1m_2m_3}, \quad (63)$$

$$\begin{aligned} c_1 &= -\frac{\alpha^4 - (\alpha - m_1)^3(\alpha + 3m_1) - (\alpha - m_2)^4 - (\alpha - m_3)^4}{4m_1A}, \\ c_2 &= -\frac{\alpha^4 - (\alpha - m_1)^4 - (\alpha - m_2)^3(\alpha + 3m_2) - (\alpha - m_3)^4}{4m_2A}, \\ c_3 &= -\frac{\alpha^4 - (\alpha - m_1)^4 - (\alpha - m_2)^4 - (\alpha - m_3)^3(\alpha + 3m_3)}{4m_3A}, \end{aligned} \quad (64)$$

where

$$A = \alpha^3 - (\alpha - m_1)^3 - (\alpha - m_2)^3 - (\alpha - m_3)^3. \quad (65)$$

Configuration 5: Quadrilateral cutting interface 2

When $m_{12} < m_3$ and $m_{12} < \alpha < 1/2$, all intercepts on x_i coordinates exceeds the range of of the hexahedron. The cutting interface is a hexagon. The cutting polyhedron can be determined by subtracting two smaller tetrahedron from the tetrahedron formed by the original ponit and three intercepts points, then combine the intersection of the two small tetrahedron. The volume and corresponding centroid are expressed as

$$V = \frac{A}{6m_1m_2m_3}, \quad (66)$$

$$\begin{aligned} c_1 &= \frac{1}{2} - \frac{m_1}{6(2\alpha - m_{12})}, \\ c_2 &= \frac{1}{2} - \frac{m_2}{6(2\alpha - m_{12})}, \\ c_3 &= \frac{3(\alpha - 2m_{12})(2\alpha - m_{12}) + \alpha m_{12} - m_1m_2}{6(2\alpha - m_{12})}, \end{aligned} \quad (67)$$

where

$$A = 3m_1m_2(2\alpha - m_1 - m_2). \quad (68)$$

Appendix B: Tables for numerical tests

Table 4: Geometrical errors in 2D Zalesak's disk rotation test when CFL number is 0.05 and 0.05, using different MOF advection methods. The data corresponds with the line plots in Fig. 7(a) and Fig. 7(b)

Resolution (N)	EI	LE	LEEI2D	EILE2D	WY
CFL = 0.05					
16	1.37E-02 <i>2.19</i>	1.37E-02 <i>2.19</i>	1.37E-02 <i>2.19</i>	1.37E-02 <i>2.19</i>	1.38E-02 <i>2.20</i>
32	3.00E-03 <i>1.40</i>	3.00E-03 <i>1.41</i>	3.00E-03 <i>1.41</i>	3.00E-03 <i>1.40</i>	3.00E-03 <i>1.40</i>
64	1.14E-03 <i>1.08</i>	1.13E-03 <i>1.13</i>	1.13E-03 <i>1.08</i>	1.14E-03 <i>1.09</i>	1.14E-03 <i>1.07</i>
128	5.38E-04 <i>0.75</i>	5.19E-04 <i>0.64</i>	5.36E-04 <i>0.67</i>	5.34E-04 <i>0.73</i>	5.39E-04 <i>0.74</i>
128	3.20E-04	3.34E-04	3.37E-04	3.22E-04	3.22E-04
CFL = 0.5					
16	1.10E-02 <i>2.03</i>	1.10E-02 <i>2.02</i>	1.10E-02 <i>2.02</i>	1.10E-02 <i>2.03</i>	1.10E-02 <i>2.02</i>
32	2.70E-03 <i>1.35</i>	2.70E-03 <i>1.35</i>	2.70E-03 <i>1.35</i>	2.70E-03 <i>1.35</i>	2.70E-03 <i>1.35</i>
64	1.06E-03 <i>1.47</i>	1.06E-03 <i>1.47</i>	1.06E-03 <i>1.47</i>	1.06E-03 <i>1.47</i>	1.06E-03 <i>1.47</i>
128	3.83E-04 <i>1.39</i>	3.83E-04 <i>1.39</i>	3.83E-04 <i>1.39</i>	3.83E-04 <i>1.39</i>	3.83E-04 <i>1.39</i>
256	1.46E-04	1.46E-04	1.46E-04	1.46E-04	1.46E-04
The computed orders of accuracy are in italics between mesh entries.					

Table 5: Geometrical errors in 2D Zalesak’s disk rotation test with a 64×64 mesh, using different MOF advection methods. The data corresponds with the line plots in Fig. 8

CFL number	EI	LE	LEEI2D	EILE2D	WY
0.05	1.14E-03	1.13E-03	1.13E-03	1.14E-03	1.14E-03
0.1	1.13E-03	1.13E-03	1.13E-03	1.13E-03	1.13E-03
0.15	1.12E-03	1.12E-03	1.12E-03	1.12E-03	1.12E-03
0.2	1.11E-03	1.11E-03	1.11E-03	1.11E-03	1.11E-03
0.25	1.11E-03	1.11E-03	1.11E-03	1.11E-03	1.11E-03
0.3	1.10E-03	1.10E-03	1.10E-03	1.10E-03	1.10E-03
0.5	1.06E-03	1.06E-03	1.06E-03	1.06E-03	1.06E-03

Table 6: Geometrical errors in 2D Rider-Kothe single vortex test with a 64×64 mesh, using different MOF advection methods. The data corresponds with the line plots in Fig. 11 (a)

CFL number	EI	LE	LEEI2D	EILE2D	WY
0.05	8.08E-03	9.28E-03	8.68E-03	9.29E-03	1.11E-02
0.1	8.51E-03	7.88E-03	8.08E-03	7.68E-03	9.46E-03
0.15	8.35E-03	7.68E-03	7.18E-03	6.45E-03	9.51E-03
0.2	9.13E-03	8.49E-03	6.19E-03	7.19E-03	9.69E-03
0.25	1.01E-02	9.46E-03	6.39E-03	7.16E-03	1.02E-02
0.3	1.16E-02	9.96E-03	6.42E-03	6.66E-03	1.07E-02
0.5	1.52E-02	1.33E-02	7.01E-03	7.23E-03	1.22E-02
0.8	2.22E-02	1.81E-02	7.63E-03	8.02E-03	1.59E-02
1.0	2.64E-02	2.13E-02	8.47E-03	8.83E-03	1.79E-02

Table 7: Mass errors in 2D Rider-Kothe single vortex test with a 64×64 mesh, using different MOF advection methods. The data corresponds with the line plots in Fig. 11(b)

CFL number	EI	LE	LEEI2D	EILE2D	WY
0.05	2.70E-03	-2.68E-03	5.00E-06	3.21E-13	3.19E-13
0.1	5.40E-03	-5.33E-03	2.20E-05	1.37E-13	1.56E-13
0.15	8.09E-03	-7.97E-03	3.00E-05	9.13E-14	1.07E-13
0.2	1.08E-02	-1.06E-02	2.90E-05	5.30E-14	8.01E-14
0.25	1.35E-02	-1.32E-02	2.70E-05	4.71E-14	6.52E-14
0.3	1.61E-02	-1.58E-02	2.60E-05	1.08E-14	5.42E-14
0.5	2.69E-02	-2.58E-02	2.10E-05	2.32E-14	3.20E-14
0.8	4.29E-02	-4.02E-02	-9.60E-05	1.51E-14	2.18E-14
1	5.35E-02	-4.93E-02	-5.40E-05	5.89E-15	1.63E-14

Table 8: Geometrical errors in 2D Rider-Kothe single vortex test when CFL number is 0.05 and 1.0, using different MOF advection methods. The data corresponds with the line plots in Fig. 12(a) and Fig. 12(c)

Resolution (N)	EI	LE	LEEI2D	EILE2D	WY
CFL = 0.05					
16	7.93E-02 <i>1.35</i>	6.39E-02 <i>0.98</i>	6.82E-02 <i>1.09</i>	6.15E-02 <i>0.62</i>	8.04E-02 <i>1.37</i>
32	3.11E-02 <i>1.94</i>	3.23E-02 <i>1.80</i>	3.20E-02 <i>1.88</i>	4.00E-02 <i>2.11</i>	3.12E-02 <i>1.49</i>
64	8.08E-03 <i>1.15</i>	9.28E-03 <i>1.08</i>	8.68E-03 <i>1.44</i>	9.29E-03 <i>1.34</i>	1.11E-02 <i>1.72</i>
128	3.64E-03 <i>1.80</i>	4.39E-03 <i>1.96</i>	3.20E-03 <i>1.61</i>	3.68E-03 <i>1.97</i>	3.37E-03 <i>1.31</i>
256	1.05E-03	1.13E-03	1.05E-03	9.41E-04	1.36E-03
CFL = 1.0					
16	7.99E-02 <i>0.54</i>	5.85E-02 <i>0.70</i>	7.68E-02 <i>1.29</i>	7.72E-02 <i>1.34</i>	8.16E-02 <i>1.02</i>
32	5.48E-02 <i>1.06</i>	3.61E-02 <i>0.76</i>	3.13E-02 <i>1.89</i>	3.04E-02 <i>1.78</i>	4.02E-02 <i>1.17</i>
64	2.64E-02 <i>1.11</i>	2.13E-02 <i>1.05</i>	8.47E-03 <i>1.58</i>	8.83E-03 <i>1.57</i>	1.79E-02 <i>0.91</i>
128	1.22E-02 <i>1.00</i>	1.03E-02 <i>1.03</i>	2.83E-03 <i>1.18</i>	2.98E-03 <i>1.23</i>	9.52E-03 <i>1.05</i>
256	6.12E-03	5.05E-03	1.25E-03	1.27E-03	4.59E-03
The computed orders of accuracy are in italics between mesh entries.					

Table 9: Mass errors in 2D Rider-Kothe single vortex test when CFL number is 0.05 and 1.0, using different MOF advection methods. The data corresponds with the line plots in Fig. 12(b) and Fig. 12(d)

Resolution (N)	EI	LE	LEEI2D	EILE2D	WY
CFL = 0.05					
16	1.19E-02	-1.23E-02	-3.67E-04	5.85E-14	1.24E-13
32	5.42E-03	-5.40E-03	-1.24E-04	2.62E-13	2.13E-13
64	2.70E-03	-2.68E-03	5.00E-06	3.21E-13	3.19E-13
128	1.35E-03	-1.34E-03	8.00E-06	2.24E-13	2.93E-13
256	6.76E-04	-6.72E-04	3.00E-06	3.58E-13	3.15E-13
CFL = 1.0					
16	2.32E-01	-2.02E-01	-2.13E-02	3.73E-15	8.64E-15
32	1.07E-01	-9.56E-02	-1.48E-03	1.06E-14	1.24E-14
64	5.35E-02	-4.93E-02	-5.40E-05	5.89E-15	1.63E-14
128	2.69E-02	-2.58E-02	6.80E-05	1.14E-14	1.90E-14
256	1.35E-02	-1.32E-02	5.10E-05	9.62E-15	2.08E-14

Table 10: Geometrical errors reconstruction in 2D reversed vortex test with a 64×64 mesh, using different MOF advection methods. The data corresponds with the line plots in Fig. 15 (b)

CFL number	EI	LE	LEEI2D	EILE2D	WY
0.05	6.96E-03	6.41E-03	6.12E-03	6.27E-03	5.88E-03
0.1	8.03E-03	6.97E-03	6.31E-03	6.55E-03	6.02E-03
0.15	8.78E-03	7.38E-03	5.92E-03	6.45E-03	6.22E-03
0.2	9.93E-03	6.82E-03	6.37E-03	6.71E-03	6.69E-03
0.25	1.10E-02	7.60E-03	6.47E-03	7.35E-03	7.09E-03
0.3	1.22E-02	7.30E-03	6.54E-03	7.85E-03	7.80E-03
0.5	1.57E-02	9.41E-03	6.46E-03	8.09E-03	9.10E-03
0.8	2.25E-02	1.26E-02	6.38E-03	9.11E-03	1.18E-02
1.0	2.65E-02	1.47E-02	7.13E-03	1.02E-02	1.43E-02

Table 11: Mass errors in 2D reversed vortex test with a 64×64 mesh, using different MOF advection methods. The data corresponds with the line plots in Fig. 15(b)

CFL number	EI	LE	LEEI2D	EILE2D	WY
0.05	-1.90E-03	1.77E-03	-1.10E-05	1.63E-14	1.06E-14
0.1	-4.01E-03	3.35E-03	-1.40E-04	-5.10E-15	6.68E-15
0.15	-6.10E-03	4.79E-03	-8.60E-05	-3.97E-14	5.10E-15
0.2	-8.47E-03	6.65E-03	-2.80E-04	4.71E-15	5.69E-15
0.25	-1.08E-02	7.91E-03	-5.23E-04	5.50E-15	5.10E-15
0.3	-1.37E-02	9.33E-03	-4.07E-04	3.73E-15	5.10E-15
0.5	-2.58E-02	1.23E-02	-9.80E-04	2.75E-15	3.93E-15
0.8	-4.71E-02	1.33E-02	-2.72E-03	7.85E-16	-2.33E-05
1	-6.75E-02	1.15E-02	-4.57E-03	1.96E-15	1.27E-03

Table 12: Geometrical errors in 2D reversed vortex test when CFL number is 0.05 and 1.0, using different MOF advection methods. The data corresponds with the line plots in Fig. 16(a) and Fig. 16(c)

Resolution (N)	EI	LE	LEEI2D	EILE2D	WY
CFL = 0.05					
16	1.80E-02 <i>0.98</i>	1.52E-02 <i>1.10</i>	1.62E-02 <i>1.10</i>	1.57E-02 <i>1.04</i>	2.24E-02 <i>1.55</i>
32	9.13E-03 <i>0.39</i>	7.08E-03 <i>0.14</i>	7.55E-03 <i>0.30</i>	7.64E-03 <i>0.28</i>	7.66E-03 <i>0.38</i>
64	6.96E-03 <i>0.30</i>	6.41E-03 <i>0.23</i>	6.12E-03 <i>0.18</i>	6.27E-03 <i>0.20</i>	5.88E-03 <i>0.08</i>
128	5.67E-03 <i>1.60</i>	5.45E-03 <i>1.63</i>	5.41E-03 <i>1.63</i>	5.45E-03 <i>1.59</i>	5.55E-03 <i>1.44</i>
256	1.87E-03	1.76E-03	1.75E-03	1.81E-03	2.05E-03
CFL = 1.0					
16	8.72E-02 <i>0.80</i>	2.71E-02 <i>0.24</i>	1.31E-02 <i>0.58</i>	3.24E-02 <i>1.30</i>	4.44E-02 <i>0.69</i>
32	5.01E-02 <i>0.92</i>	2.29E-02 <i>0.64</i>	8.72E-03 <i>0.29</i>	1.32E-02 <i>0.36</i>	2.75E-02 <i>0.95</i>
64	2.65E-02 <i>0.74</i>	1.47E-02 <i>0.66</i>	7.13E-03 <i>0.20</i>	1.02E-02 <i>0.44</i>	1.43E-02 <i>0.72</i>
128	1.59E-02 <i>1.29</i>	9.32E-03 <i>0.94</i>	6.20E-03 <i>1.57</i>	7.57E-03 <i>1.68</i>	8.69E-03 <i>1.24</i>
256	6.49E-03	4.87E-03	2.09E-03	2.35E-03	3.68E-03
The computed orders of accuracy are in italics between mesh entries.					

Table 13: Mass errors in 2D reversed vortex test when CFL number is 0.05 and 1.0, using different MOF advection methods. The data corresponds with the line plots in Fig. 16(b) and Fig. 16(d)

Resolution (N)	EI	LE	LEEI2D	EILE2D	WY
CFL = 0.05					
16	2.61E-03	-2.34E-03	1.92E-03	5.89E-15	1.49E-14
32	-3.34E-03	3.28E-03	7.42E-04	1.65E-14	3.46E-14
64	-1.90E-03	1.77E-03	-1.10E-05	1.63E-14	1.06E-14
128	-9.91E-04	9.66E-04	1.20E-05	1.63E-14	1.98E-14
256	-5.26E-04	5.49E-04	3.50E-05	2.75E-14	3.30E-14
CFL = 1.0					
16	-6.13E-01	-1.49E-01	-6.26E-02	9.82E-16	-3.23E-03
32	-1.94E-01	-1.52E-02	-8.40E-03	1.96E-15	2.04E-03
64	-6.75E-02	1.15E-02	-4.57E-03	1.96E-15	1.27E-03
128	-2.65E-02	1.16E-02	-7.68E-04	1.96E-16	2.41E-04
256	-1.28E-02	8.58E-03	3.37E-04	1.77E-15	1.85E-04

Table 14: Geometrical errors in 3D Zalesak's test when CFL number is 0.3, using different MOF advection methods. The data corresponds with the line plots in Fig. 18

Resolution (N)	EI	LE	EILE3D	EILE3DS	EIEALE	WY
16	1.23E-02	1.23E-02	1.27E-02	1.23E-02	1.22E-02	1.22E-02
	<i>1.54</i>	<i>1.54</i>	<i>1.52</i>	<i>1.54</i>	<i>1.53</i>	<i>1.53</i>
32	4.22E-03	4.22E-03	4.46E-03	4.22E-03	4.23E-03	4.23E-03
	<i>1.73</i>	<i>1.73</i>	<i>1.73</i>	<i>1.73</i>	<i>1.74</i>	<i>1.74</i>
64	1.27E-03	1.27E-03	1.35E-03	1.27E-03	1.27E-03	1.27E-03
	<i>1.08</i>	<i>1.08</i>	<i>0.97</i>	<i>1.08</i>	<i>1.07</i>	<i>1.07</i>
128	6.03E-04	6.03E-04	6.86E-04	6.03E-04	6.02E-04	6.02E-04

The computed orders of accuracy are in italics between mesh entries.

Table 15: Geometrical errors in 3D Zalesak’s test with a $64 \times 64 \times 64$ mesh, using different MOF advection methods. The data corresponds with the line plots in Fig. 19

	EI	LE	EILE3D	EILE3DS	EIEALE	WY
0.05	1.51E-03	1.51E-03	1.67E-03	1.51E-03	1.51E-03	1.51E-03
0.1	1.40E-03	1.40E-03	1.51E-03	1.40E-03	1.40E-03	1.40E-03
0.15	1.35E-03	1.35E-03	1.44E-03	1.35E-03	1.35E-03	1.35E-03
0.2	1.31E-03	1.31E-03	1.40E-03	1.31E-03	1.31E-03	1.31E-03
0.25	1.29E-03	1.29E-03	1.37E-03	1.29E-03	1.29E-03	1.29E-03
0.3	1.27E-03	1.27E-03	1.35E-03	1.27E-03	1.27E-03	1.27E-03
0.5	1.20E-03	1.20E-03	1.29E-03	1.20E-03	1.20E-03	1.20E-03

Table 16: Geometrical errors in 3D single vortex test with a $32 \times 32 \times 64$ mesh, using different MOF advection methods. The data corresponds with the line plots in Fig. 23 (a)

CFL number	EI	LE	EILE3D	EILE3DS	EIEALE	WY
0.05	3.20E-03	3.18E-03	2.83E-03	3.19E-03	3.16E-03	3.21E-03
0.1	3.46E-03	3.04E-03	2.71E-03	3.16E-03	3.26E-03	3.06E-03
0.15	3.91E-03	3.20E-03	2.87E-03	3.00E-03	3.11E-03	3.14E-03
0.2	4.38E-03	3.15E-03	3.03E-03	3.14E-03	3.12E-03	3.18E-03
0.25	4.88E-03	3.26E-03	3.05E-03	3.17E-03	3.13E-03	3.22E-03
0.3	5.30E-03	3.36E-03	3.12E-03	3.27E-03	3.34E-03	3.40E-03
0.5	7.40E-03	4.17E-03	7.60E-02	3.88E-03	3.85E-03	3.92E-03
0.8	1.01E-02	5.72E-03	1.72E-01	4.72E-03	4.76E-03	4.85E-03
1	1.13E-02	6.74E-03	2.14E-01	5.49E-03	5.75E-03	5.78E-03

Table 17: Mass errors in 3D single vortex test with a $32 \times 32 \times 64$ mesh, using different MOF advection methods. The data corresponds with the line plots in Fig. 28 (b)

CFL number	EI	LE	EILE3D	EILE3DS	EIEALE	WY
0.05	1.33E-02	-1.33E-02	3.10E-13	-1.50E-05	5.04E-07	2.98E-14
0.1	2.68E-02	-2.62E-02	1.73E-13	-2.50E-05	2.32E-06	1.50E-14
0.15	4.06E-02	-3.86E-02	1.36E-13	3.33E-04	4.89E-06	3.56E-14
0.2	5.38E-02	-5.14E-02	9.48E-14	-9.60E-05	1.90E-06	2.65E-14
0.25	6.70E-02	-6.35E-02	8.15E-14	-1.81E-04	3.63E-06	2.15E-14
0.3	8.11E-02	-7.40E-02	6.67E-14	4.59E-04	9.18E-06	2.48E-14
0.5	1.34E-01	-1.19E-01	-1.02E+01	-8.59E-04	-1.73E-05	1.63E-14
0.8	2.13E-01	-1.77E-01	-2.37E+01	-1.84E-03	-2.71E-04	-5.72E-04
1	2.67E-01	-2.10E-01	-2.95E+01	-2.69E-03	-1.89E-04	-3.36E-04

Table 18: Geometrical errors in 3D single vortex test with a $64 \times 64 \times 64$ mesh, using different MOF advection methods. The data corresponds with the line plots in Fig. 24 (a) and Fig. 24 (c)

Resolution (N)	EI	LE	EILE3D	EILE3DS	EIEALE	WY
<hr/>						
CFL = 0.3						
<hr/>						
16	9.68E-03 <i>0.20</i>	9.85E-03 <i>0.60</i>	1.01E-02 <i>0.53</i>	1.11E-02 <i>0.75</i>	1.18E-02 <i>0.85</i>	9.37E-03 <i>0.49</i>
32	8.45E-03 <i>0.67</i>	6.50E-03 <i>0.95</i>	6.98E-03 <i>1.16</i>	6.60E-03 <i>1.01</i>	6.54E-03 <i>0.97</i>	6.67E-03 <i>0.97</i>
64	5.30E-03 <i>0.96</i>	3.36E-03 <i>1.15</i>	3.12E-03 <i>1.18</i>	3.27E-03 <i>1.25</i>	3.34E-03 <i>1.28</i>	3.40E-03 <i>1.29</i>
128	2.73E-03	1.51E-03	1.37E-03	1.37E-03	1.38E-03	1.39E-03
<hr/>						
CFL = 1.0						
<hr/>						
16	1.04E-02 <i>0.02</i>	1.24E-02 <i>0.74</i>	1.05E-01 <i>0.27</i>	1.19E-02 <i>0.67</i>	1.14E-02 <i>0.58</i>	1.14E-02 <i>0.56</i>
32	1.02E-02 <i>0.47</i>	7.47E-03 <i>0.84</i>	8.72E-02 <i>0.20</i>	7.48E-03 <i>0.95</i>	7.57E-03 <i>0.98</i>	7.74E-03 <i>0.98</i>
64	7.40E-03 <i>0.82</i>	4.17E-03 <i>1.03</i>	7.60E-02 <i>0.10</i>	3.88E-03 <i>1.13</i>	3.85E-03 <i>1.09</i>	3.92E-03 <i>1.11</i>
128	4.18E-03	2.04E-03	7.06E-02	1.78E-03	1.81E-03	1.81E-03
<hr/>						
The computed orders of accuracy are in italics between mesh entries.						
<hr/>						

Table 19: Mass errors in 3D single vortex test when CFL number is 0.05 and 1.0, using different MOF advection methods. The data corresponds with the line plots in Fig. 24(b) and Fig. 24(d)

Resolution (N)	EI	LE	EILE3D	EILE3DS	EIEALE	WY
CFL = 0.5						
16	5.34E-01	-5.48E-01	-1.32E+01	5.83E-02	-3.50E-03	-6.13E-16
32	2.82E-01	-2.59E-01	-1.13E+01	1.05E-03	-6.16E-04	6.50E-15
64	1.34E-01	-1.19E-01	-1.02E+01	-8.59E-04	-1.70E-05	1.63E-14
128	6.43E-02	-5.99E-02	-9.74E+00	-2.96E-04	3.70E-05	3.66E-14
CFL = 1.0						
16	8.26E-01	9.04E-02	-2.86E+01	2.53E-01	-2.71E-02	-9.19E-02
32	5.46E-01	-3.09E-01	-3.09E+01	2.59E-02	-5.68E-03	2.59E-03
64	2.67E-01	-2.10E-01	-2.95E+01	-2.69E-03	-1.89E-04	-3.36E-04
128	1.29E-01	-1.13E-01	-2.88E+01	-1.30E-03	4.28E-04	6.01E-04

Table 20: Geometrical errors in 3D reversed vortex test with a $64 \times 64 \times 64$ mesh, using different MOF advection methods. The data corresponds with the line plots in Fig. 28 (a)

CFL number	EI	LE	EILE3D	EILE3DS	EIEALE	WY
0.05	2.20E-03	2.19E-03	2.28E-03	2.19E-03	2.18E-03	2.18E-03
0.1	2.19E-03	2.17E-03	2.21E-03	2.15E-03	2.12E-03	2.12E-03
0.15	2.31E-03	2.26E-03	2.19E-03	2.20E-03	2.18E-03	2.18E-03
0.2	2.39E-03	2.30E-03	2.28E-03	2.27E-03	2.21E-03	2.22E-03
0.25	2.50E-03	2.36E-03	2.30E-03	2.35E-03	2.26E-03	2.32E-03
0.3	2.64E-03	2.45E-03	2.37E-03	2.42E-03	2.35E-03	2.34E-03
0.5	3.16E-03	2.81E-03	2.56E-03	2.74E-03	2.57E-03	2.58E-03
0.8	4.01E-03	3.53E-03	2.98E-03	3.30E-03	2.98E-03	3.01E-03
1	4.57E-03	4.11E-03	3.28E-03	3.69E-03	3.34E-03	3.35E-03

Table 21: Mass errors in 3D reversed vortex test with a $64 \times 64 \times 64$ mesh, using different MOF advection methods. The data corresponds with the line plots in Fig. 28 (b)

CFL number	EI	LE	EILE3D	EILE3DS	EIEALE	WY
0.05	3.95E-03	-3.95E-03	1.67E-13	3.00E-06	6.24E-08	1.41E-13
0.1	7.89E-03	-7.90E-03	6.60E-14	1.30E-05	3.50E-07	7.89E-14
0.15	1.18E-02	-1.19E-02	7.48E-14	2.70E-05	1.10E-06	5.84E-14
0.2	1.58E-02	-1.58E-02	5.44E-14	5.40E-05	2.09E-06	4.88E-14
0.25	1.97E-02	-1.98E-02	4.85E-14	8.10E-05	3.99E-06	3.47E-14
0.3	2.36E-02	-2.37E-02	4.21E-14	1.08E-04	7.46E-06	2.88E-14
0.5	3.93E-02	-3.95E-02	2.86E-14	3.25E-04	3.69E-05	2.26E-14
0.8	6.26E-02	-6.33E-02	1.40E-14	8.46E-04	1.61E-04	1.48E-05
1	7.80E-02	-7.90E-02	1.94E-14	1.33E-03	3.81E-04	1.71E-04

Table 22: Geometrical errors in 3D reversed vortex test with a $64 \times 64 \times 64$ mesh, using different MOF advection methods. The data corresponds with the line plots in Fig. 29 (a) and Fig. 29 (c)

Resolution (N)	EI	LE	EILE3D	EILE3DS	EIEALE	WY
CFL = 0.3						
16	1.11E-02 <i>0.70</i>	9.83E-03 <i>0.65</i>	1.03E-02 <i>0.70</i>	1.04E-02 <i>0.71</i>	1.04E-02 <i>0.71</i>	1.06E-02 <i>0.79</i>
32	6.83E-03 <i>1.37</i>	6.26E-03 <i>1.35</i>	6.32E-03 <i>1.42</i>	6.35E-03 <i>1.40</i>	6.33E-03 <i>1.43</i>	6.11E-03 <i>1.39</i>
64	2.64E-03 <i>1.85</i>	2.45E-03 <i>1.96</i>	2.37E-03 <i>2.10</i>	2.42E-03 <i>2.02</i>	2.35E-03 <i>2.11</i>	2.34E-03 <i>2.10</i>
128	7.32E-04	6.29E-04	5.50E-04	5.97E-04	5.43E-04	5.44E-04
CFL = 1.0						
16	1.35E-02 <i>0.75</i>	1.23E-02 <i>0.77</i>	1.04E-02 <i>0.90</i>	1.15E-02 <i>0.90</i>	1.07E-02 <i>0.86</i>	1.10E-02 <i>0.94</i>
32	8.03E-03 <i>0.81</i>	7.24E-03 <i>0.82</i>	5.55E-03 <i>0.76</i>	6.12E-03 <i>0.73</i>	5.91E-03 <i>0.82</i>	5.69E-03 <i>0.77</i>
64	4.57E-03 <i>1.30</i>	4.11E-03 <i>1.36</i>	3.28E-03 <i>1.53</i>	3.69E-03 <i>1.44</i>	3.34E-03 <i>1.54</i>	3.35E-03 <i>1.54</i>
256	1.86E-03	1.60E-03	1.13E-03	1.36E-03	1.15E-03	1.16E-03
The computed orders of accuracy are in italics between mesh entries.						

Table 23: Mass errors in 3D reversed vortex test when CFL number is 0.05 and 1.0, using different MOF advection methods. The data corresponds with the line plots in Fig. 29(b) and Fig. 29(d)

Resolution (N)	EI	LE	EILE3D	EILE3DS	EIEALE	WY
CFL = 0.3						
16	9.53E-02	-9.70E-02	1.50E-14	1.93E-03	9.00E-06	1.39E-14
32	4.73E-02	-4.76E-02	3.34E-14	3.90E-04	1.50E-05	2.21E-14
64	2.36E-02	-2.37E-02	4.21E-14	1.08E-04	7.00E-06	2.88E-14
128	1.18E-02	-1.19E-02	6.39E-14	2.70E-05	4.00E-06	3.12E-14
CFL = 1.0						
16	2.95E-01	-3.07E-01	7.36E-15	2.84E-02	-2.33E-04	-6.57E-04
32	1.54E-01	-1.55E-01	1.34E-14	5.66E-03	5.23E-04	-2.20E-05
64	7.80E-02	-7.90E-02	1.94E-14	1.33E-03	3.81E-04	1.71E-04
128	3.93E-02	-3.96E-02	7.90E-14	3.17E-04	2.00E-04	1.19E-04